Identification of the dual roles of Al_2O_3 coatings on NMC811-cathodes *via* theory and experiment

RLB Chen[1,2], FN Sayed[1,2], H Banerjee[1,2,3], I Temprano[1,2,4], AJ Morris[2,5], CP Grey[1,2*]

[1]*Yusuf Hamied Department of Chemistry, University of Cambridge, Cambridge CB2 1EW, U.K.*
[2]*The Faraday Institution, Didcot OX11 0RA, U.K.*
[3]*School of Science and Engineering, University of Dundee, Dundee, DD1 4HN, Scotland, U.K.*
[4]*CICA - Interdisciplinary Center for Chemistry and Biology, University of A Coruña, 15071, A Coruña, Spain.*
[5]*School of Metallurgy and Materials, University of Birmingham, Birmingham, B15 2TT, U.K.*
**Corresponding author: cpg27@cam.ac.uk*

Abstract

Metal-oxide coatings are a favoured strategy for mitigating surface degradation problems in state-of-the-art lithium-ion battery Ni-rich layered positive electrode materials. Despite their extensive use, a full, fundamental understanding of the role of coatings in reducing degradation and extending cycling lifetimes is currently lacking. In this work, the interactions between an atomic layer deposited (ALD) alumina coating on polycrystalline $LiNi_{0.8}Mn_{0.1}Co_{0.1}O_2$ (NMC811) and a carbonate-based battery electrolyte are studied. Solid-state nuclear magnetic resonance (ssNMR) heteronuclear experiments show that the Al_2O_3 coating transforms by reacting with electrolyte species present before and during electrochemical cycling, scavenging protic and acidic species. Density-functional theory calculations highlight the additional chemical effect of the coating in locally stabilising the structure of the NMC811, limiting oxidation of the oxygen atoms coordinated to both Al and Ni, thereby limiting the surface reconstruction process and improving the electrochemical performance. Improved NMC811 surface stability is confirmed by monitoring gaseous degradation species by *operando* electrochemical mass-spectrometry and *via* X-ray spectroscopic analysis of the electrochemically aged samples to examine changes in Ni and O oxidation state and local structure. The combination of this experimental and theoretical analysis suggests that Al_2O_3 coatings have a dual role: as a protective barrier against attack from chemical species in the electrolyte, and as an artificial passivating layer hindering oxygen loss and surface phase transformations. This holistic approach, which provides a fundamental understanding of how the surface stability is improved by the coating, will aid the design of the state-of-the-art and future positive electrode materials.

Introduction

Ni-rich layered oxide positive electrode materials such as $LiNi_xMn_yCo_zO_2$ ($x > 0.6$, $y < 0.2$ and $z = 1 - x - y$; NMC*xyz*) are the state-of-the-art choice for the positive electrode in high-energy density rechargeable Li-ion batteries and used in the electrification of vehicles.[1–3] However, accessing the higher energy density comes with challenges, affecting the lifetime and safety of these materials; this includes cracking of the secondary particles (the agglomerates of primary nanoparticles that are present in polycrystalline NMC samples),[4–6] increased reactivity with electrolytes, which leads to cross-talk of transition metals (TM)[7–9] and electrolyte degradation species,[8,10] and surface and sub-surface phase changes (for example, reconstruction of the surface layered structure to rock salt), following reactions that in general increase impedance.[11–13] One proposed strategy for addressing these surface degradation phenomena in Ni-rich layered materials is to modify the NMC surfaces with a thin layer of metal oxide such as Al_2O_3.[14–16]

Al_2O_3 coatings improve the capacity retention during electrochemical cycling and improve the rate performance of high Ni NMC materials.[17–19] However, a fundamental understanding of the mechanism is lacking – in particular, the structural evolution of Al_2O_3 on electrochemical cycling and its impact on the NMC particle surface and sub-surface is unclear. Moreover, the variety of coating methods adds uncertainty to the analysis of the coating's function. Coating methods include wet-chemistry based processes like solution deposition[20–22] or sol-gel[23–25], dry coating processes[26–29] and deposition processes such as atomic layer deposition (ALD).[30–32] Compared with wet-chemistry based methods, in which the subsequent annealing temperature determines the structure and uniformity of the coating and doping into the subsurface,[33] ALD offers a route to synthesise nanometre thin, highly conformal, continuous and dense coatings even when the underlying host material has a complex surface morphology.[16,30,34–36] A carefully controlled coating limited to the surface is advantageous when deconvoluting the mechanisms behind the protective effect of the coating.

Al_2O_3 coatings on NMC811 (by ALD) extend the lifetime and reduce the growth in charge-transfer resistance impedance.[14,16] This improvement in electrochemical cycling performance is concomitant with mitigated layered-to-rock salt transformation (surface reconstruction) of the NMC811 as seen in the Ni *L*-edge and O *K*-edge electron energy loss spectroscopy (EELS) of electrodes in the discharged state after extended cycling.[14] That is, the layered structure of NMC811 is well-preserved by the coating, resulting in little chemical difference in the Ni-O bonding environment between Ni on the surface and sub-surface of a particle.[14] However, different findings were seen in Ni *K*-edge X-ray absorption spectroscopy (XAS) of layered oxides charged to high states-of-charge (SoC)[37] – the Ni edge energy of Ni ions close

to the surface (approximately ~20 nm) was not seen to shift to the higher energies seen for the Ni in the sub-surface (~150 nm), even when an Al_2O_3 coating was present. The authors concluded that the surface Ni, susceptible to surface reconstruction, was not oxidised to the same extent as bulk Ni and this instability was not improved by coating with Al_2O_3.

Whilst these previous X-ray spectroscopy studies have characterised the surface transition metal chemistry of layered oxides to understand the effect of coatings on surface degradation, changes to the chemical environment of the coating were not clearly identified. Analysing the evolution of the coating with solid-state nuclear magnetic resonance (ssNMR) could reveal unique insights into its function. ssNMR is sensitive to the local chemical and structural environments around an observed spin (*i.e.* ^{27}Al), allowing structural characterisation of the different Al coordination environments found in Al_2O_3 coatings[38] to be linked to the electrochemical performance of the coated Ni-rich layered oxide.[39–42] Post-mortem analysis of Al_2O_3 coated NMC after electrochemical cycling with ssNMR to determine the role of the coating has been more scarce in the literature. The ^{27}Al spectra in past studies[40,43] suggest that little structural and chemical evolution of the Al_2O_3 coating have occurred, in contrast to reported HF scavenging reactions that might be expected to occur given the degradation mechanisms proposed in the literature.[44–48] It should be noted that these ^{27}Al spectra were measured on coatings deposited using wet-chemistry methods where the “bulk” alumina signals likely dominate the signal rather than the signals from alumina surface species. The use of double-resonance NMR experiments, not widely employed to study these systems, provides a strategy to obtain more detailed local chemical information. For example, the proximity of ^{7}Li to ^{27}Al spins in Al-F based coatings deposited by ALD, as found in ^{27}Al{^{7}Li} and ^{7}Li{^{19}F} rotational echo double resonance (REDOR) NMR experiments, suggest the formation of a lithiated coating.[42]

In this study we characterise the ALD Al_2O_3 coatings formed on polycrystalline NMC811 and how the coatings evolve with cycling. This is achieved by using a combination of single and double-resonance ssNMR experiments that monitor the local coordination environment of Al, measuring gaseous and solution electrolyte degradation species arising from NMC811-electrolyte interactions at high potentials, and density functional theory using a Hubbard correction (DFT+U) to examine the surface Ni/O electronic states to explore improved capacity retention and surface stability. The coating is shown to have a dual protective role: namely, the coating plays a key role in scavenging electrolyte decomposition species (from the commonly used $LiPF_6$-based carbonates) and in stabilising the surface oxygen of NMC811.

Experimental methods

(i) Materials

Commercial polycrystalline NMC811 (Targray) stored in an Ar-filled glovebox (GB, MBraun, Germany; O_2 and H_2O < 0.1 ppm) was used as a baseline material. The polycrystalline NMC811 powders were coated by Forge Nano *via* a proprietary ALD process after keeping the powders at 120 ^oC overnight in a fluidised reactor bed. The ALD reaction proceeded at 120 ^oC in the same reactor bed with cycles of trimethyl aluminium (TMA) precursor gas followed by water vapour and then purging with N_2 – the resulting concentration of Al after coating the NMC811 was 223 ppm (baseline powder, uncoated, had 34 ppm of Al) as determined by inductively coupled plasma mass spectrometer (ICP-MS). Powders were transported under N_2 before taking them into the Ar-filled glovebox (GB). The polycrystalline Al_2O_3-coated NMC811 is referred to as ALD NMC811 herein.

(ii) Characterisation of the pristine powders

ALD Al_2O_3 coated and uncoated NMC811 powders were pressed onto carbon tape for scanning electron microscopy (SEM) or onto carbon-coated Cu grids for transmission electron microscopy (TEM) imaging inside the Ar-filled glovebox but samples were briefly exposed to air during loading into the microscopes. SEM (TESCAN MIRA3 FEG-SEM) coupled with energy-dispersive x-ray spectroscopy (EDX) mapping (5.0 kV operating voltage) was used for elemental analysis – at least 8 area scans for 3 different secondary particles were averaged to obtain a representative value. TEM (Thermo Scientific Talos F200X G2 TEM) coupled with EDX mapping was also performed at 200 kV for elemental comparisons (averaged across 3 secondary particles) between the edge and bulk (100 - 200 nm further in) regions of the secondary particle.

X-ray powder diffraction patterns collected at RT on a PANalytical Empyrean diffractometer (Cu Kα irradiation, $\lambda = 1.5406$ Å with a Ni filter) for the uncoated NMC811 and the ALD Al_2O_3 coated NMC811 (material just referred to as ALD NMC811 henceforth). Rietveld refinements[49] were performed with Academic TOPAS (v.6.1) software[50] to obtain structural parameters and determine bulk structural changes, if any, after the coating process. A $R\bar{3}m$ space group with transition metals (TM) at the *3a* Wyckoff positions, Li on the *3b* sites and O on the *6c* sites was used with the oxygen positions, lattice parameters and Li/TM anti-site occupancies being allowed to iterate (details in ES1). Displacement parameters were assumed isotropic and given values of 1.

(iii) Soaking experiments of the pristine material

For soaking experiments of the pristine material, ethylene carbonate (EC) and ethyl methyl carbonate (EMC) (EC:EMC = 3:7 (v/v), SoulBrain MI) solvents and lithium hexafluorophosphate ($LiPF_6$) salt (Solvionic, 99.99%) were used. Polypropylene vials were initially dried at 60 ^oC before transferring into the glovebox to reduce introduced moisture. 30 mg of active material (ALD NMC811 or uncoated NMC811) were soaked for 24 h in 600 µL of either the EC/EMC solvent or freshly mixed 1 M $LiPF_6$ in EC/EMC electrolyte. After soaking, 400 µL of the solvent (electrolyte) was pipetted out for analysis by ^1H and ^{19}F solution NMR using a C_6D_6 capillary for shift referencing to avoid any contamination from trace H_2O in deuterated solvents. The remaining solvent (electrolyte) was pipetted out and the residual slurry was rinsed with excess dimethyl carbonate (DMC, Sigma- Aldrich, anhydrous, ≥ 99%) before drying *in-vacuo*. After drying, the NMC811 powders were packed for ssNMR measurements in 1.3 mm rotors. All sample handling was done inside the Ar GB.

(iv) Assembly of Swagelok cells for solid-state NMR

Ex-situ ssNMR studies were performed after electrochemical cycling on materials (without binder and current collector to minimise background signals) in oven-dried Swagelok cells. ALD NMC811 and the Super P conductive carbon were dried at 120 ^oC under vacuum before being mixed (80:20 wt%) using an agate mortar and pestle (dried at 100 ^oC in a vacuum oven prior to use) inside the Ar GB. This mixture was transferred into a ½-inch swagelok cell with the cell stack and completed with borosilicate glass fibre separators (Whatmann, GF/B, 0.68 mm thick, 1 µm pore size, dried at 120 ^oC for 12 h under vacuum) flooded with freshly mixed 300 µL of 1 M $LiPF_6$ in EC/EMC electrolyte and a Li metal disk (12 mm diameter; MTI Corporation, 99.9%). The inside of the cell was lined with Kapton polyimide film (DuPont) film to ensure that no loose positive electrode powder would be displaced and come into direct contact with the Li metal leading to a short circuit. The entire Swagelok cell was (dis)assembled inside the Ar GB. After electrochemical cycling, the positive electrode powder mix was soaked in 1 mL DMC for 5 min before *in-vacuo* drying. Analogous cells with the uncoated NMC811 were also (dis)assembled for electrochemical cycling comparisons. Details of coin cell preparation for electrochemistry and *ex-situ* experiments are in provided in **ESI 2: Fabrication of coin cells.**

(v) Electrochemical measurements

Electrochemical cycling of (*ALD*) *NMC811*|Li Swagelok cells was performed on a MPG2 potentiostat (Biologic) using the EC-lab software at room temperature (RT, 20 ± 2 °C). The cell was rested for 4 h at the open-circuit voltage before galvanostatic (dis)charging at C/20 to different cut-off voltages (assuming a practical capacity of 200 $mAhg^{-1}$). A potentiostatic hold

was applied at the upper cut-off voltage (4.4 V_{Li}) until the current decayed to the C/40 value to account for Li-ion concentration gradients in the NMC811 particles.

Electrochemical cycling of *LFP*|Li and (*ALD*) *NMC811*|delithiated LFP coin cells was performed on a BT-2000 potentiostat (Arbin) running the MITS Pro software at RT. *LFP*|Li cells were rested for 4 h before galvanostatic charging at a C/20 rate (practical capacity of 127 $mAhg^{-1}$) to 4.0 V_{Li} with a hold until the current decays to the C/40 value followed by galvanostatic discharge until 3.8 V_{Li} and were then disassembled for the delithiated LFP. (*ALD*) *NMC811*|delithiated LFP cells were rested for 4 h before C/10 charging (assuming a practical capacity of 200 $mAhg^{-1}$) up to 1.16 V (~4.6 V_{Li}). The cells were held at this potential for 60 h before C/10 galvanostatic discharge -0.46 V (~3.0 V_{Li}) with this protocol being repeated for 5 cycles.

Electrochemical cycling of *NMC811*|graphite coin cells were performed on a BT-2000 potentiostat at RT. Cells were first charged to 1.5 V at C/20 (assuming 200 $mAhg^{-1}$ practical capacity) and held for 15 min before resting at OCV for 6 h to passivate the Cu current collector of the graphite. Cells underwent formation cycles (C/20) between 2.5 – 4.3 V for 2 cycles to form a stable SEI on the graphite and diagnose the available capacity. Extended electrochemical cycling was conducted over 1040 cycles in sets with each set consisting of 48 ageing C/2 cycles (UCV holds until the current decays to the C/20 value) followed by 3 diagnostic C/20 cycles (UCV holds until the current decays to C/40). All *NMC811*|Li cells (with pristine or aged electrodes) were charged to 4.4 V_{Li} with a UCV hold until the current value decayed to the C/100.

(vi) Solid state NMR characterisation

^{1}H rotor-synchronised Hahn-echo ($\frac{\pi}{2} - \tau - \pi - \tau -$acquire) NMR experiments under magic-angle spinning (MAS, 50 kHz) conditions were acquired at 16.4 T using a Bruker 1.3 mm double-resonance (DR) probe. Excitation was achieved with 125 kHz applied radio frequency (rf) field strength *i.e.* π pulse of 4 μs. Evolution and refocusing times, τ, were set to five rotor periods to filter out broad background signals (with fast spin-spin T_2 relaxation), and a recycle delay of 1 s was used. ^{1}H chemical shifts were referenced externally to the lower frequency peak of adamantane (1.85 ppm).

^{19}F Hahn-echo NMR experiments were acquired at 4.7 T with a 1.3 mm DR probe whilst spinning with a MAS frequency of 50 kHz (1.3 mm rotor). ^{19}F pulses of 263 kHz rf field strength, τ was one rotor period and 250 ms recycle delays were used. ^{19}F chemical shifts were referenced externally to AlF_3 (-172.0 ppm).

^{27}Al Hahn-echo NMR experiments were acquired at either 23.5 T with a 1.9 mm triple resonance (TR) probe at a 40 kHz MAS frequency and 156 kHz rf field strength or at 16.4 T with a 1.3 mm DR probe at a 50 kHz MAS frequency and 179 kHz rf field strength. A $\frac{\pi}{6}$ pulse length is normally used to excite all environments with different quadrupolar couplings uniformly and be quantitative.[51] However, the short pulse length results in lower excitation compared to $\frac{\pi}{2}$ pulses so to achieve sufficient signal-to-noise ratio (SNR) in these very low Al concentration samples, longer $\frac{\pi}{3}$ pulse lengths at the cost of being fully quantitative. 75 ms recycle delays were used (see **ESI 3: Details about NMR parameters** for further details about additional recycle delay times). ^{27}Al chemical shifts were referenced externally to AlF_3 (-17 ppm).

Double resonance REDOR and TRAPDOR experiments[52,53] were also used to obtain detailed chemical information – signal attenuation indicates that two spins (different elements) are in close proximity. Calibration curves were first performed on Gibbsite $Al(OH)_3$, α-AlF_3 and γ-$LiAlO_2$ to determine appropriate dipolar evolution times – experimental times on the samples take ~3 days per spectrum, ruling out obtaining a full REDOR curve for the sample. Further experimental details on the double resonance experiments can be found in **ESI 4: Experimental details for double resonance experiments.**

(vii) Solution state NMR characterisation

Cycled *(ALD) NMC811*|LFP coin cells were disassembled in the Ar GB and the glass fibre soaked in 1 mL of DMSO-d_6 (Sigma-Aldrich, 99.9 atom % D, 99 % CP) for 5 min. 0.7 mL of solution was then transferred to an NMR tube fitted with a J-Young tap.

One-dimensional ^{1}H and ^{19}F{^{1}H} NMR spectra and two-dimensional ^{1}H-^{1}H correlation spectroscopy (COSY) were collected at 11.7 T (500 GHz ^{1}H Larmor frequency) on a Bruker AVANCE III HD spectrometer with a BBO probe. ^{1}H was referenced internally to the DMSO-d_6 solvent at 2.50 ppm whilst ^{19}F was referenced internally to $LiPF_6$ at -74.5 ppm.

(viii) On-line electrochemical mass spectrometry (OEMS)

Gas evolution from *(ALD) NMC811*|Li cells with 1 M $LiPF_6$ in EC:EMC (3:7, v/v) electrolyte were investigated using OEMS. The experimental setup has previously been described elsewhere.[54,55] The cell is cycled using an Ivium Vertex potentiostat with the following protocol: 6 h rest at OCV, C/10 galvanostatic charge to 4.6 V_{Li} coupled with a potential hold at 4.6 V_{Li} for 1 h, C/10 galvanostatic discharge until 3.0 V_{Li}, an OCV rest for 2 h and then the cycle is repeated at C/5.

(ix) X-ray Absorption Spectroscopy (XAS)

XAS measurements on the *NMC811*|Li samples charged to 4.4 V_{Li} were conducted at the I09 beamline using the total electron yield (TEY) mode. All transition metal *L*-edge spectra were background corrected with a straight-line baseline and then normalised to the L_3 pre-peak intensity. O *K*-edge spectra on the other hand was only baseline corrected with a straight line through the pre-peak region and then normalised to the pre-peak at ~528.0 eV seen in a reference commercial $LiNiO_2$ (BASF).

(x) First-principles calculations

First-principles calculations were carried out on the plane-wave basis as implemented in the Vienna Ab-initio Simulation Package (VASP)[56,57] version 5.4 with Projector-Augmented Wave (PAW)[58] potential. The exchange-correlation functional was chosen to be that of Generalised Gradient Approximation (GGA) implemented following the Perdew–Burke–Ernzerhof[59] prescription for solids (PBESol).[60] For ionic relaxations, the internal positions of the atoms were allowed to relax until the forces became less than 0.005 eV/Å. An energy cutoff of 550 eV, and 8 × 8 × 1 Gamma centred k-point mesh (for the slab calculations with vacuum on top) were found to provide a good convergence of the total energy in self-consistent field calculations.

The NMC811 cell was constructed based on a 5 x 4 x 1 supercell of the rhombohedral $LiNiO_2$ (LNO) unit cell. In each layer 2 Ni ion was replaced by Mn and 2 by Co, with all dopant atoms surrounded only by Ni atoms, and the maximum possible separation between dopant ions in each layer possible within the supercell was considered, to prevent unphysical clustering of dopant ions. 75 % of the Li was removed from the pristine NMC811 structure to achieve an experimentally relevant state of 75 % delithiation, and both pristine as well as 75 % delithiated structures were studied to decouple the effects of coating from the effects of delithiation. Three different structures were created, in each case, each with a vacuum of ~20 Å along the *b* direction to mimic the effect of a coated/uncoated surface. One structure was uncoated, and the surface was left exposed to vacuum, while in the other two structures, surface TM atoms were partially (56.25 %) and fully replaced by Al atoms to mimic the effect of a coating on the surface. These structures were fully relaxed using the PBESol functional,[60] as it is considered to reproduce the experimental lattice constants of solids accurately. The choice of the surface was motivated by the active surface chosen in a previous study by Genreith Schriever *et al*,[61] who showed that the O loss was most profound in the (*012*) facet of LNO. In this case, the plane perpendicular to the *b*-direction is chosen as it is analogous to the (*012*) plane in this rhombohedral unit cell.

To account for the correlation effects at Ni, Mn, and Co sites beyond GGA, a Hubbard U correction was incorporated (following the DFT+U as implemented by Liechtenstein et al.)[62], where we use a Hubbard interaction parameter of U_{Ni} = 6 eV, U_{Mn} = 4.5eV, and U_{Co} = 5eV and a uniform Hund's coupling parameter J = 0.75 eV. Integrated crystal orbital Hamilton population (ICOHP)[63] were calculated based on the LOBSTER[64] package to estimate the Ni-O hybridisation in each case. O *p* charges were calculated following the Bader charge partitioning method.[65]

Results

1. Characterisation of the Coating

(i) The Al_2O_3 coated NMC811: Microscopy and diffraction

To confirm the successful deposition of an Al-based coating and identify the morphology and structure of the NMC811, particles are first imaged with electron microscopy and their diffraction patterns are collected. The SEM (**Figure 1** (**a** - **b**)) demonstrates that the secondary particle morphology (spherical agglomerates of primary nanocrystals) of the NMC811 is well-preserved after the ALD process.

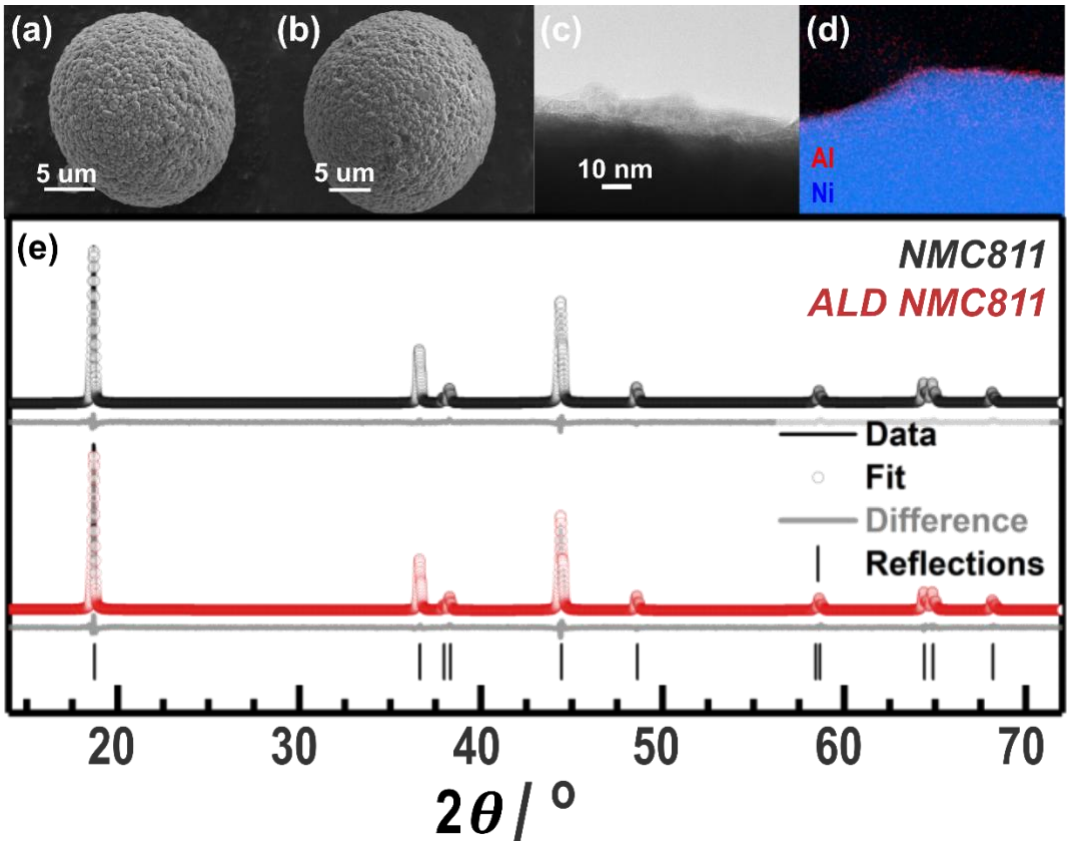

Figure 1: SEM images of the as-synthesised (a) NMC811 and (b) the ALD NMC811 secondary particles. High-resolution (HR) TEM image of the (c) ALD NMC811 particle with a corresponding EDX map of Ni (blue) and Al (red) for the (d) ALD NMC811 particle. The X-ray (λ = 1.5406 Å) diffraction patterns (e) of the NMC811 (black) and ALD NMC811 (red) are compared, showing the experimental data (solid line), the Rietveld refinement (open

circles), the difference between the data and fit (grey line) and the position of the expected reflections of the $R\bar{3}m$ space group (vertical ticks).

Closer inspection with HR-TEM (**Figure 1** (**c**)) coupled with EDX mapping (**Figure 1** (**d**)) shows that the coating (~1 nm thick) has a disordered structure that is conformal to the secondary particles. Crystalline fringes in the NMC811 particle indicate the ordered, repeating transition metal layers of the layered oxide structure. Overlaying the Al elemental map with the Ni shows that the Al is concentrated at the edge of the particle, supporting the assignment of the Al_2O_3 coating being surface-limited. The microscopy observation agrees with ICP-MS measurements, whereby the ALD NMC811 has an Al concentration (by weight) of 223 ppm which indicates successful coating (34 ppm for the baseline NMC811 with no coating). A detailed structural analysis of the disordered coating is performed below with NMR (**Figure 2**).

XRD analysis (**Figure 1** (**e**) and **Table S1**) of the powders confirms that the bulk crystal structure is unaffected by the coating process, where the *a*- and *c*- lattice parameters from Rietveld refinements of the ALD NMC811 and uncoated NMC811 were 2.8715(3) Å, 14.205(2) Å and 2.8716(3) Å, 14.205(2) Å respectively. Therefore, any changes to the NMC811 electrochemical performance must be due to the presence of the coating.

(ii) NMR to chemically characterise the coating and interactions with the electrolyte

The disordered Al-based coating (seen in TEM (**Figure 1** (**c**)) and its interactions with the electrolyte are first characterised with NMR. Revealing structural changes in the absence of electrochemical cycling provides a foundation for understanding the effect of the coating on cycling performance.

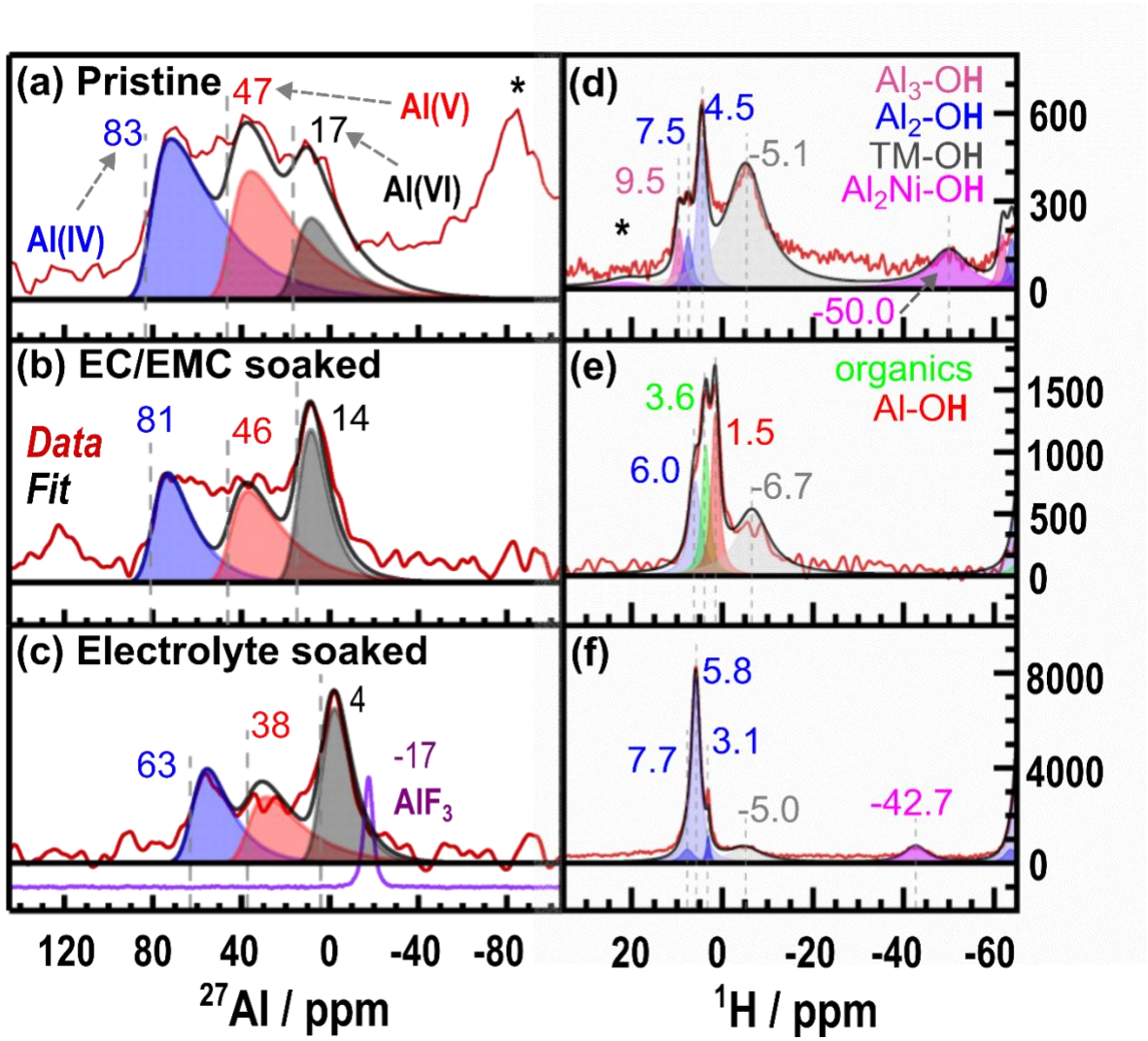

*Figure 2: ^{27}Al MAS NMR spectra of the ALD NMC811 in the (a) as-synthesised/pristine state, (b) the material after soaking in the EC/EMC (3:7 (v/v)) solvent for 24 h (then dried under vacuum) and (c) the material after soaking in 1 M $LiPF_6$ in the EC/EMC (3:7 (v/v)) electrolyte for 24 h (then dried under vacuum). The spectrum from a reference AlF_3 with a chemical shift at -17 ppm is included. The spectrum obtained in (a) was acquired at 23.5 T whilst spectra in (b) and (c) were acquired at 16.4 T. Spectra were fitted using Czjzek models and the Al(IV), Al(V) and Al(VI) components are plotted in blue, red and black respectively (fits found in **ESI 5: Supporting NMR experiments**). The grey dashed lines mark the average isotropic chemical shift extracted from the fits; these are offset from the centre of mass due to the second order quadrupolar interaction. Mass-normalised ^{1}H MAS NMR spectra of ALD NMC811 in the (d) pristine state, (e) the ALD NMC811 after soaking in the EC/EMC solvent for 24 h and (f) the ALD NMC811 after soaking in 1M $LiPF_6$ in the EC/EMC electrolyte for 24 h. Spectra are fitted with Gaussian/Lorentzian line shapes and incorporate chemical shift anisotropy to model spinning sidebands (see **ESI 5: Supporting NMR experiments** for further fitting details). Isotropic chemical shifts of each fitted component are marked with a dashed line. Spinning sidebands are marked with asterisks (*).*

^{27}Al NMR of the pristine ALD NMC811 in **Figure 2** (**a**) shows that the coating consists of tetrahedral (Al(IV)), penta-coordinated (Al(V)) and octahedral (Al(VI)) local environments for the Al^{3+} ions. The presence of the Al(V) environments and broad peaks indicate an amorphous or disordered phase[66] (in agreement with the TEM in **Figure 1** (**c**)) meaning each type of environment will have a distribution of second order quadrupolar interactions and isotropic chemical shifts, resulting in the asymmetric lineshape with a tail at lower chemical shifts. The size of the quadrupolar interaction, C_Q, measures the interaction between the local electric

field gradient and the quadrupole and is therefore indicative of local distortions around the Al^{3+} ions – this interaction is reduced at higher magnetic field strengths. Quadrupolar nuclei in disordered solids can be fit with a Czjzek model; where the distribution of quadrupolar interactions and isotropic chemical shifts are given by averaged values ($\bar{C}_Q$ and $\bar{\delta}_{iso}$ respectively).[67,68] Fitting the spectrum with a Czjzek model (see **ESI 5: Supporting NMR experiments** for the fit parameters) gives approximate proportions for Al(IV):Al(V):Al(VI) of 47:37:16 whilst the grey dashed lines in the spectrum indicate the extracted average isotropic chemical shifts of each Al environment ($\bar{\delta}_{iso,IV}$= 83 ppm, $\bar{\delta}_{iso,V}$= 47 ppm and $\bar{\delta}_{iso,VI}$= 17 ppm). The fit in the Al(IV) region in particular is poor and there are likely further species at lower frequencies (but still in the chemical shift range of Al(IV)). A range of possible Al(IV) sites (with chemical shifts ranging from 50 – 100 ppm) was observed in our previous work investigating amorphous ALD alumina deposited on a silicon wafer – the Al(IV) region was dominated by signals at a lower frequency of ~70 ppm[38] and could justify the inclusion of other Al(IV) components in the fitting in **Figure 2** (**a**). In this previous work,[38] the Al(IV):Al(V):Al(VI) proportion in the ALD alumina deposited on a silicon wafer was approximately 50:38:12 which gives similar populations of Al environments to the ALD alumina-coated NMC811 studied in this work. No Al signal was observed at negative frequencies (~-900 ppm)[69,70] in the region expected for Al substitution in the bulk[69,70] indicating that the ALD process does not result in any Al doping into the NMC811 crystal structure.

Exposing ALD NMC811 to the EC/EMC carbonate-based solvent (**Figure 2** (**b**)) shows that the saturated Al(VI) coordination environments increase at the expense of the undercoordinated Al(IV) sites (*i.e.* Al(IV):Al(V):Al(VI) changes to 32:36:32). However, the chemical shifts remain similar to the pristine case with $\bar{\delta}_{iso,IV}$ = 81 ppm, $\bar{\delta}_{iso,V}$ = 46 ppm and $\bar{\delta}_{iso,VI}$ = 14 ppm. When the material is exposed to the electrolyte ($LiPF_6$ in EC/EMC), Al environments show a similar proportion of environments (**Figure 2** (**c**)) to the EC/EMC soaked sample (Al(IV):Al(V):Al(VI) now 31:30:39). However, the ^{27}Al NMR shows on average lower chemical shifts of $\bar{\delta}_{iso,IV}$ = 63 ppm, $\bar{\delta}_{iso,V}$ = 38 ppm and $\bar{\delta}_{iso,VI}$ = 4 ppm. These changes indicate the coating is affected by both, the solvent (salt-free soaking in **Figure 2** (**b**)) and salt components of the electrolyte (**Figure 2** (**c**)), but in different ways.

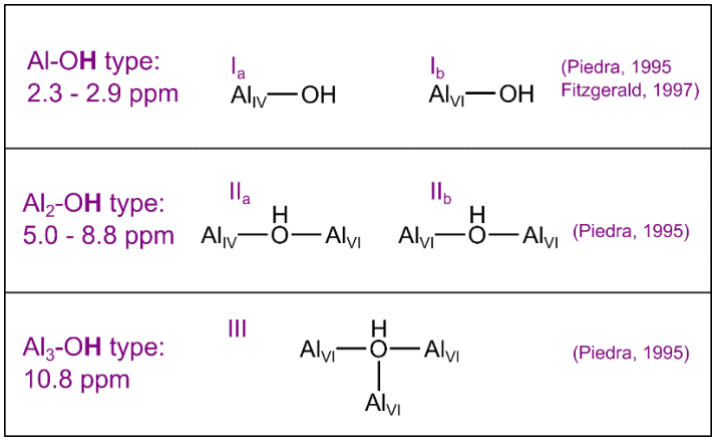

Scheme 1: The five different types of hydroxylated Al environments on the surface of γ-Al_2O_3 proposed by Peri.[71] *The references mentioned have assigned chemical shifts for these environments based on experimental data: Piedra et al.*[72] *and Fitzgerald et al.*[73] *Al_{IV} denotes Al with tetrahedral coordination whilst Al_{VI} denotes octahedral coordination.*

The relation between Al and H at the surface, before and after the material is soaked in EC/EMC solvent (or the $LiPF_6$ in EC/EMC) is probed with ^{1}H NMR. To separate out the species (and respective resonances) not associated with the coating, the ^{1}H spectrum of the uncoated NMC811 (**Figure S7**) was first fit. Three diamagnetic resonances were seen at 1.2 (most likely grease from glove-box or tentatively terminal TM-OH groups with hydrogen bonding), 3.8 (tentatively organic carbonates, 3.6 – 4.5 ppm[8,10] or physisorbed water) and 6.1 ppm (tentatively lithium bicarbonate). Additional broad features centred around -5.0 – -6.7 ppm (tentatively ascribed to OH groups nearby a TM ion)[74] and -93.2 ppm (Ni_2M-OH groups where M=TM or Al ions, based on the shifts seen for layered nickel metal hydroxides)[75,76] are observed, with further discussion on their assignment in **ESI 5: Supporting NMR experiments**. On the other hand, three different diamagnetic resonances related to the Al_2O_3 coating are observed at 4.5, 7.5 and 9.5 ppm in pristine ALD NMC811 (**Figure 2** (**d**)). Previous NMR characterisation of aluminium oxide hydroxide and aluminium hydroxide phases[72,73,77] has shown that protic species nearby Al can have a range of chemical shifts from approximately 2.3 ppm for terminal OH groups and in the range 5.5 – 10.8 ppm for protons on bridging oxygens (Al-O-Al/Al_2-O or Al_2-O-Al/Al_3-O) with hydrogen bonding (**Scheme 1**). Therefore, the ^{1}H resonances at 7.5 and 9.5 ppm of the amorphous Al_2O_3 coating are tentatively assigned to OH groups chemisorbed to Al (Al_2-OH and Al_3-OH respectively). ^{1}H resonances at around 4.8 ppm are normally assigned to the bulk water[78,79] but based on the ^{1}H{^{27}Al} TRAPDOR experiment below, the resonance at 4.5 ppm for the coating appears to contain a contribution from an Al-bonded OH. In amorphous aluminium hydroxides, bound OH groups have previously been reported at 4.5 ppm whilst physisorbed water on these aluminium hydroxides had a resonance around 5 ppm.[77] A broad paramagnetic resonance is also observed at -50.0 ppm which is tentatively assigned to Al_2Ni-OH environments.[75,80] The ^{27}Al{^{1}H} REDOR spectra for the pristine ALD NMC811 (**Figure S9** (**a**)) shows an overall

attenuation in signal intensity of the Al(IV), Al(V) and Al(VI) environments. This indicates that at least a subset of Al^{3+} ions in all three Al coordination environments are experiencing dipolar interactions with ^{1}H and are thus nearby protons. The REDOR experiments are supported by $^{1}H\{^{27}Al\}$ TRAPDOR (**Figure S9** (**b**)) experiments showing the influence of ^{1}H-^{27}Al dipolar coupling on the ^{1}H spectrum: two dominant peaks (4.9 and 9.5 ppm) are seen in the TRAPDOR difference spectrum along with a broad peak at -7.0 ppm. Therefore, these resonances belong to protic species that are located within a few Å to Al^{3+} cations. Furthermore, these experiments suggest that the broad peaks at -5 to -7 ppm are likely due to alumina environments nearby both paramagnetic and Al ions, possibly in configurations involving H-bonding to an oxygen nearby a TM or in environments such as (NiMnAl)-OH (see SI); the difference in chemical shift between the peak at 4.5 ppm of the Hahn-echo experiment (**Figure 2** (**d**)) and the peak in the difference spectrum of the $^{1}H\{^{27}Al\}$ TRAPDOR at 4.9 ppm (**Figure S9** (**b**)) suggests that there may be more components (configurations of Al_2-OH) than fit but see further discussion in SI.

EC/EMC solvent-soaked ALD NMC811 shows an evolution of ^{1}H signals likely resulting from reactions between trace water in the solution and the undercoordinated Al(IV) and Al(V) sites in the Al_2O_3 coating, increasing the proportion of Al(VI) sites without significantly changing the chemical shift (**Figure 2** (**b**)). This is correlated with the increase in overall ^{1}H signal intensity of the spectrum (**Figure 2** (**e**)), three new resonances appearing at 1.5, 3.6 and 6.0 ppm. Probing the ^{27}Al-^{1}H dipolar interactions with $^{27}Al\{^{1}H\}$ REDOR (**Figure S9** (**c**)) shows that (at least some of) the species giving rise to the Al(VI) signal are closer to protons than the Al(IV) and Al(V) environments. Thus the growth of the Al(VI) sites, with adsorption of protons, is concomitant with a decrease in the undercoordinated Al environments. The difference spectrum of the $^{1}H\{^{27}Al\}$ TRAPDOR experiment (**Figure S9** (**d**)) shows two distinct (5.8 and 1.4 ppm) resonances that can be matched to those found in the Hahn-echo experiment (**Figure 2** (**e**)). Therefore, the resonance at 5.8 ppm is tentatively assigned to Al_2OH like clusters with hydrogen bonding between Al_2OH groups whilst the 1.4 ppm is assigned to terminal Al-OH groups based on the chemical shifts discussed above. The resonance at 3.6 ppm in the Hahn-echo spectrum (**Figure 2** (**e**)) was not clearly observed in the TRAPDOR difference experiment (**Figure S9** (**d**)) so is assigned to the organic carbonates as for the uncoated NMC811 samples (**Figure S7**). Analysis of the EC/EMC solvent with ^{1}H solution NMR (**Figure S10**), after soaking the (un)coated NMC811 powder for 24h, shows a reduction in normalised signal intensity ascribed to water in the solvent. This supports the assertion that chemisorption of trace water occurs on soaking and results in an increase in ^{1}H signal intensity of the ALD NMC sample.

The diamagnetic ^{1}H environment (**Figure 2** (**f**)) of the ALD NMC811 material continues to evolve after soaking in the electrolyte, with an increase in the ^{1}H signal intensity of the resonances at 3.1, 5.8 and 7.7 ppm. ^{27}Al{^{1}H} REDOR (**Figure S9** (**a**)) show that (some of the) Al(VI) sites are still protonated whilst ^{1}H{^{27}Al} TRAPDOR (**Figure S9** (**b**)) verifies the persistence of $Al_2O\underline{H}$ species. The same three resonances are observed in the difference spectrum with the range in chemical shifts indicating that $Al_2O\underline{H}$ types of protons can be structurally different. However, these ^{1}H-^{27}Al heteronuclear experiments do not explain the origin of the decrease in the ^{27}Al chemical shifts observed for the electrolyte-soaked ALD NMC811 material. This indicates that the Al_2O_3 coating also interacts with the $LiPF_6$ salt (or its products) in the electrolyte. $LiPF_6$ readily undergoes hydrolysis to form HF[81,82] and this acid can react with the Al_2O_3 or the NMC811.[44–46,48] Unsurprisingly, the ^{19}F NMR spectra (**Figure S15**) of the pristine ALD NMC811 and EC/EMC-soaked material show no resonances; *i.e.* no fluorine-containing surface species are observed. In the electrolyte soaked ALD NMC811 (point *I* in **Figure 3** (**a**)), the resonances are assigned to residual $LiPF_6$ salt (-76 – -80 ppm),[8,10,81] difluorophosphate species from hydrolysis of the salt (-88 ppm)[10], an aluminium oxyfluoride species (-184 ppm),[83] and LiF (-206 ppm).[83] Fluorination of the Al_2O_3 coating could explain the decrease in ^{27}Al chemical shifts of the electrolyte-soaked ALD NMC811 (**Figure 2** (**c**), *e.g.* $\bar{\delta}_{iso,VI} = 4$ ppm) but the extent of fluorination does not reach AlF_3 ($\delta_{VI} =$ -17 ppm). ^{27}Al{^{19}F} REDOR (**Figure S13** (**c**)) shows a decrease in the signal of the Al (VI) intensity when the ^{19}F irradiation is applied during the dipolar evolution. This supports the proposed fluorination of the coating; further investigation of the ^{19}F-^{27}Al dipolar interactions with ^{19}F{^{27}Al} TRAPDOR (**Figure S13** (**d**)) was not possible due to the poor signal to noise.

In conclusion, exposure of the ALD-coated NMC811 surface to the electrolyte results in a reduction of the concentration of lower-coordinated (and more reactive) Al sites, along with partial fluorination of the coating. Fluorination is ascribed to reactions of the hydroxyl/water groups in the coating and trace water in the electrolyte with $LiPF_6$ generating species (such as HF) that can react with the undercoordinated Al sites.

2. Electrochemical cycling of ALD NMC811

(i) Cycling vs. Li metal

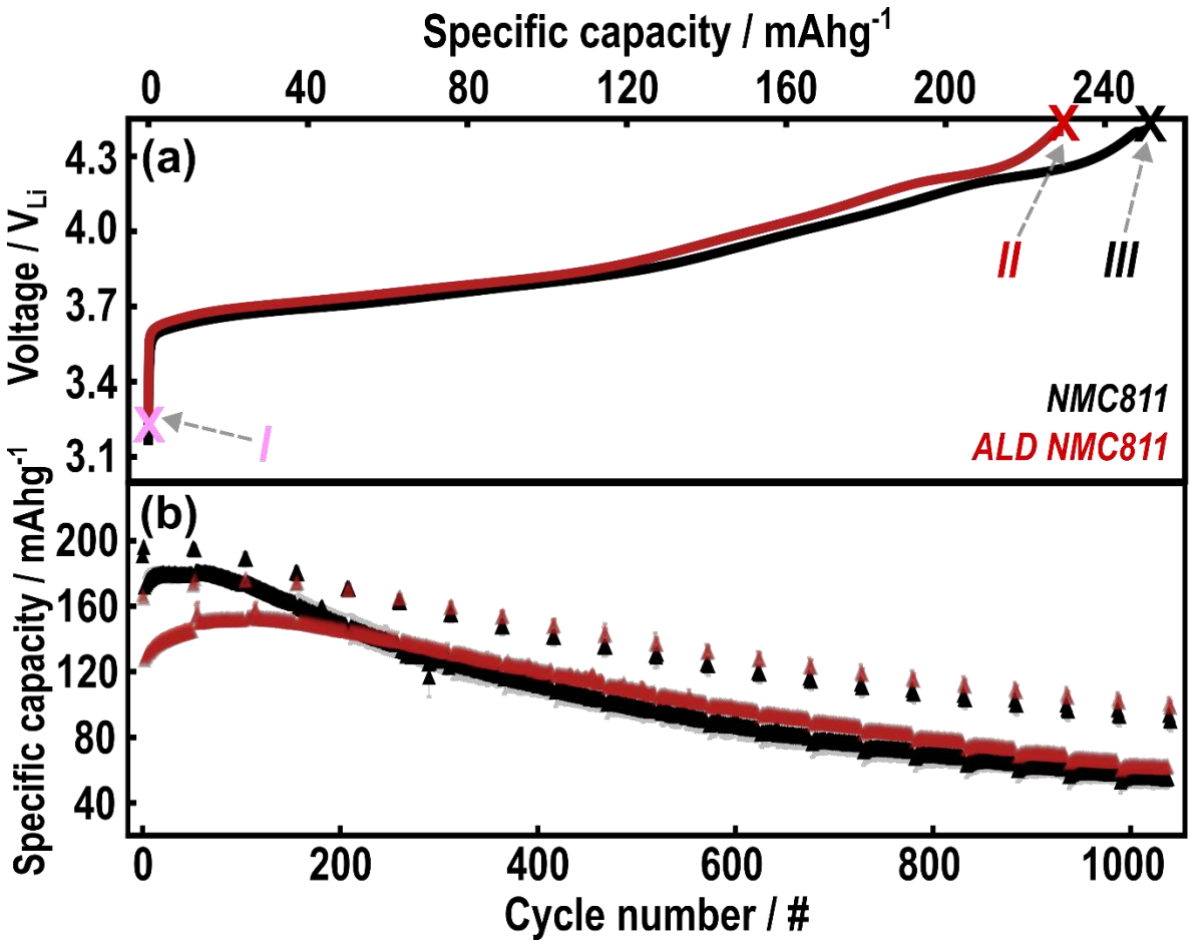

Figure 3: (a) Voltage profile of the first charge (C/20 rate assuming 200 mAhg^{-1} practical capacity) for NMC811 (black) and ALD NMC811 (red) where crosses indicate sample states analysed with post-mortem NMR: pink cross (I) indicates the ALD NMC811 soaked in 1 M $LiPF_6$ in EC/EMC, the red cross (II) indicates the ALD NMC811 charged to 4.4 V_{Li} (rinsed with DMC), and the black cross (III) is the NMC811 charged to 4.4 V_{Li} (rinsed with DMC). Discharge capacities over long-term cycling in sets of 49x ageing cycles at C/2 and 2x diagnostic cycles at C/20 are presented in (b) for the NMC811 and ALD NMC811.

Whilst the HF scavenging reaction is chemical in nature, electrochemical cycling of NMC811 has been observed to generate water from the chemical oxidation of carbonate solvents at high potentials (> 4.3 V_{Li}),[8,9,84] which can lead to $LiPF_6$ salt degradation. *ALD NMC811* | Li cells (binder-free) were charged up to 4.4 V_{Li} at a C/20 to simulate operating conditions of high energy density cells. **Figure 3 (a)** shows that the voltage profile of ALD NMC811 on charging has the same voltage slopes and plateaus as the uncoated NMC811, *i.e.* the NMC811 still undergoes its known solid-solution delithiation behaviour. However, the presence of the coating introduces an overpotential, which decreases the accessible capacity for the same C/20 charge rate.

Further binder-free (*i.e.*, initially fluorine-free) samples were then prepared to assess the evolution of coating structure as a function of state-of-charge (SoC) using NMR spectroscopy.

One sample was discharged until 3.0 V_{Li} after reaching an upper cut-off voltage of 4.4 V_{Li} (point *IV* in **Figure S17**) whilst a second sample was charged back to 4.4 V_{Li} after one cycle (3.0 – 4.4 V_{Li}, point *V* in **Figure S17**). This subsequent discharge and charge continue to show the typical voltage-capacity profile during (de-)lithiation of NMC811 and indicates unchanged solid-solution behaviour of the bulk structure as seen with other Al_2O_3 coated Ni-rich NMCs.[14,33]

(ii) Impact of the coating on long-term electrochemical performance

Electrochemical cycling to a high cut-off potential of 4.3 V (~4.4 V_{Li}) for 1042 cycles was performed using ALD NMC811 and NMC811 *vs.* a graphite negative electrode. A vinylene carbonate additive in the electrolyte was used to stabilise the SEI of the negative electrode and ensure the capacity loss is mainly attributed to the high potential degradation processes outlined above. In the electrochemical ageing of the NMC811|graphite cells (**Figure 7** (**a**) and **Table S14**), the lower initial discharge capacity of the ALD NMC811 (168 $mAhg^{-1}$) compared to the NMC811 (193 $mAhg^{-1}$) is attributed to the overpotential of the Al_2O_3 coating as seen in the first cycle voltage profile (**Figure 3** (**a**)). However, after electrochemical ageing (**Figure 7** (**a**) and **Table S14**), the Al_2O_3 coating enables higher capacity retention after 1042 cycles (101 $mAhg^{-1}$ (60 % of the initial capacity) in the ALD NMC811 compared to 94 $mAhg^{-1}$ (49 % of the initial capacity) in the NMC811). Reduced capacity fading of the NMC811 due to the coating is confirmed by the discharge capacity observed in diagnostic cells reassembled with the aged positive electrode but now with a Li electrode and fresh electrolyte to replenish the Li inventory (120 $mAhg^{-1}$ (71 % of the initial capacity) for ALD NMC811 compared to 99 $mAhg^{-1}$ (51 % of the initial capacity) for NMC811, **Table S14**).

3. Analysis of Cycled Samples – Theory and Experiment

(i) Electronic structure: Density of States and Bader charge analysis

First-principles calculations with density functional theory were pursued to examine the root-causes for less chemical oxidation observed with the electrolyte solvents. Three different supercell structures of NMC811 were created (**Figure S21**) and in each case, a vacuum of ~20 Å was applied along the *b*-direction to mimic the effect of the (010) surface. One structure was uncoated and the surface was left exposed to vacuum, whilst in the other two structures, surface Ni atoms along the (010) plane were partially (56.25 %) and fully substituted with Al atoms for one layer (extending ~1.7 Å beneath the surface). These structures are terminated on the (010) facet with oxygen ends and one exposed cation. Two scenarios for each structure are considered – fully lithiated supercells and supercells with 75 of the Li removed to simulate high SoC. This treatment of the surface is an approximation of the interface between the amorphous alumina coating and the bulk NMC crystal given that the ssNMR spectra shows that the coating structure is amorphous and modelling amorphous structure is non-trivial.

Observing the average O electronic density of states (DOS) (**Figure S22**) in the supercell shows a large contribution from O *p* orbitals near the Fermi energy due to hybridisation with Ni *d* orbitals. No significant difference in the average O *p* orbital populations, which are dominated by O in the bulk structure, for these (de-)lithiated structures are observed between the uncoated, partially coated and fully coated cases. This highlights that Al present at the surface does not influence the electronic structure of bulk oxygen. This is further demonstrated by calculated averaged crystal orbital overlap population (COOP) values, in which lower values indicate relatively higher covalency in the average Ni-O bonds of the bulk of the (de-)lithiated structures. Both the pristine as well as the 75 % delithiated case were analysed using averaged COOP values for NiO_6 octahedra in the bulk of the structures. Average COOP values for Ni-O bonds in the uncoated, 56.25 % partly coated, and fully coated NMC811 structures with full Li inventories are 1.93, 1.95, and 1.92 respectively. Average COOP values of 2.87, 2.86, and 2.86 are obtained for Ni-O bonds after 75 % delithiation in the uncoated, 56.25 % coated, and 100 % coated NMC811 structures respectively. The comparisons show that coating the surface has a negligible effect on the average Ni-O bonds within the bulk structure (~1.93) but there is a significant increase in covalency on charging (~2.87). Similar conclusions can be drawn from charge analysis of oxygen in the NMC811 structure. For example, Wannier projections of LNO (end member of Ni-rich NMC)[61] have indicated that the charge on O is closer to $2s^2\ 2p^{5.5}$ (*i.e.* 7.5 e^-) due to covalency and charge transfer (from O *p* orbitals to Ni *d* orbitals) as opposed to 8 e^- for an idealised O^{2-} ($2s^2\ 2p^6$). Given that the VASP software only considers the valence shell and Bader charge partitioning is more simplistic than Wannier projections, the estimated Bader charges are 7 e^- for the bulk oxygen (< 5 Å below the surface) in the fully lithiated NMC811 (irrespective of any coating, **Figure 4 right**). Delithiating the structures results in a decrease in average Bader charge (6.75 e^-) that can be explained by oxidation/ligand hole formation on the O 2*p* orbitals of the hybridised Ni 3*d* – O 2*p* bond at high SoC as calculated in LNO.[61,85] Bader charge densities on the surface O *p* orbitals are discussed below.

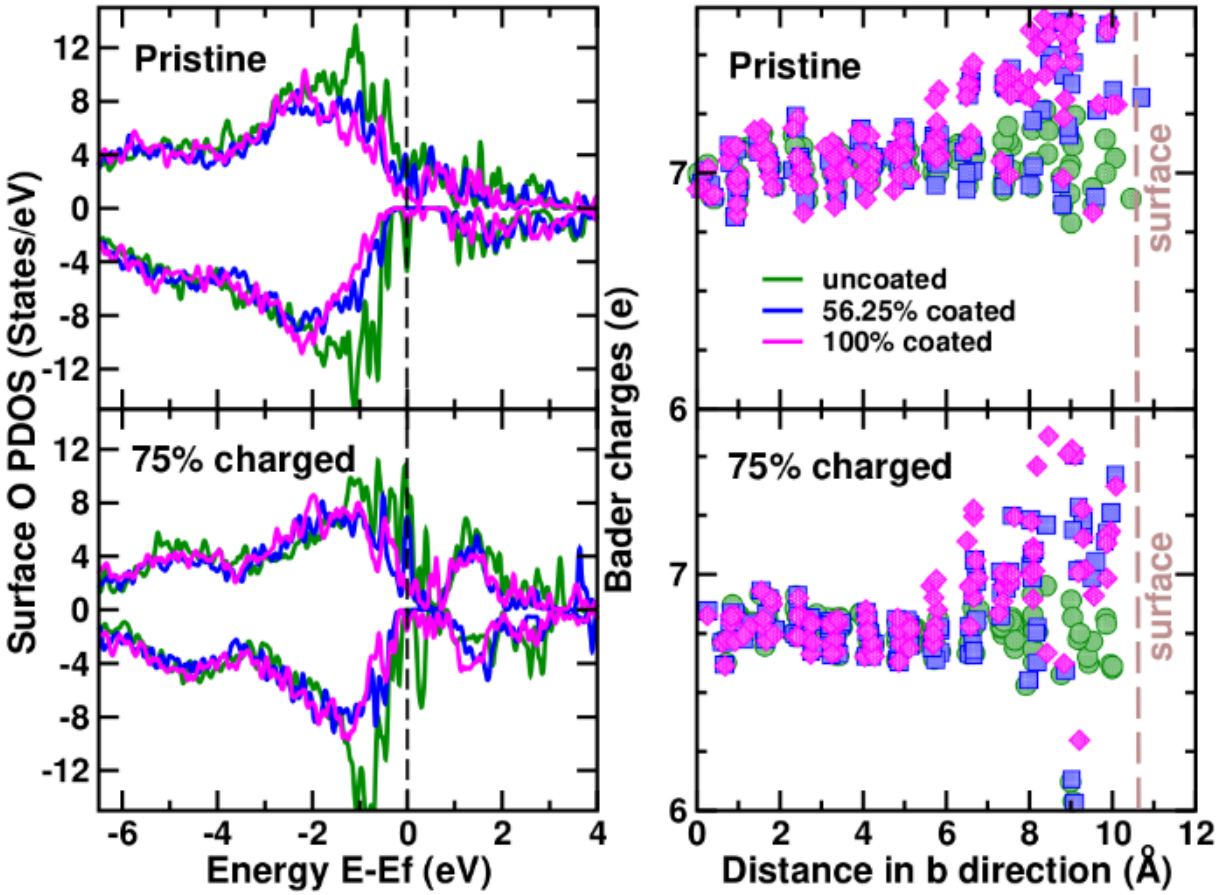

Figure 4: Electronic density of states and Bader charges: the Projected DOS (PDOS, left panel) for surface oxygens in both pristine and 75 % delithiated (charged) NMC811 structure with either no Al present (green), Al partially (56.25 %) substituting the surface transition metals (blue) or fully substituting the surface transition metals (purple). A vacuum (extending up to 20 Å) above the surface in the b-direction is applied to the surface. The black dashed line indicates the Fermi energy. On the other hand, the right panels show the Bader charges as a function of distance in the b-direction going from the bulk (0 Å) to the surface (10.8 Å, marked by the brown dashed line). The charges of the valence electrons around an idealised O^{2-} would give 8 electrons but is underestimated in Bader partitioning (ranging from ~7 in the bulk for the fully lithiated structure to ~6.75 in the bulk of the delithiated case).

The effect of the coating is seen in the projected DOS (obtained by projection of DOS onto scaled spherical harmonics in VASP) of the surface monolayer of oxygen atoms bonded to the coating layer (**Figure 4, left**). For the uncoated NMC811, a large population of O *p* orbitals is filled near the Fermi energy – indicative of the hybridisation with Ni *d* orbitals. However, in both the fully lithiated and 75 % delithiated cases of the 56.25 % coated and the 100 % coated structure, there is a significant decrease in energy states near the Fermi energy, and a shift of surface O DOS to lower energies is observed. Increasingly filled lower energy states of O *p* orbitals, as Al substitutes Ni, imply a lower degree of hybridisation with the Ni *d* orbitals, and a higher and more stable oxidation state of O. Incidentally, computed electronic DOS of amorphous Al_2O_3 in our previous work[38] indicated that the material is a wide bandgap insulator. The Al-bonding results in the O *p* orbitals of the valence and conduction bands being well separated (~2.6 eV) and this trend is mirrored in the change in surface O DOS for these Al_2O_3 coated NMC. Looking at the Bader charge of O near the surface (from 6 – 10.8 Å at the very

surface, **Figure 4 right**) shows an increase in charge density, compared to the bulk oxygen anions, when the Al is present in either partially or fully coated structures. This confirms the highly local effect that Al has on decreasing Ni *d* – O *p* orbital hybridisation in both the fully lithiated and 75 % delithiated structures.

The formation of ligand holes in LNO[86] and NMC[87] has previously been proposed as being responsible for the redox of the oxygen into an unstable peroxide state that leads to O gas loss at high SoC and concomitant surface reconstruction from the layered to rock salt structure.[61,85] Therefore, the action of Al in locally increasing the charge around O (reduced Ni 3*d* – O 2*p* hybridisation) suggests that coatings using Al have an additional effect of improving the resilience of NMC811 against oxidation of surface O to reactive oxygen species.

(ii) NMR characterisation of electrochemically cycled ALD NMC811

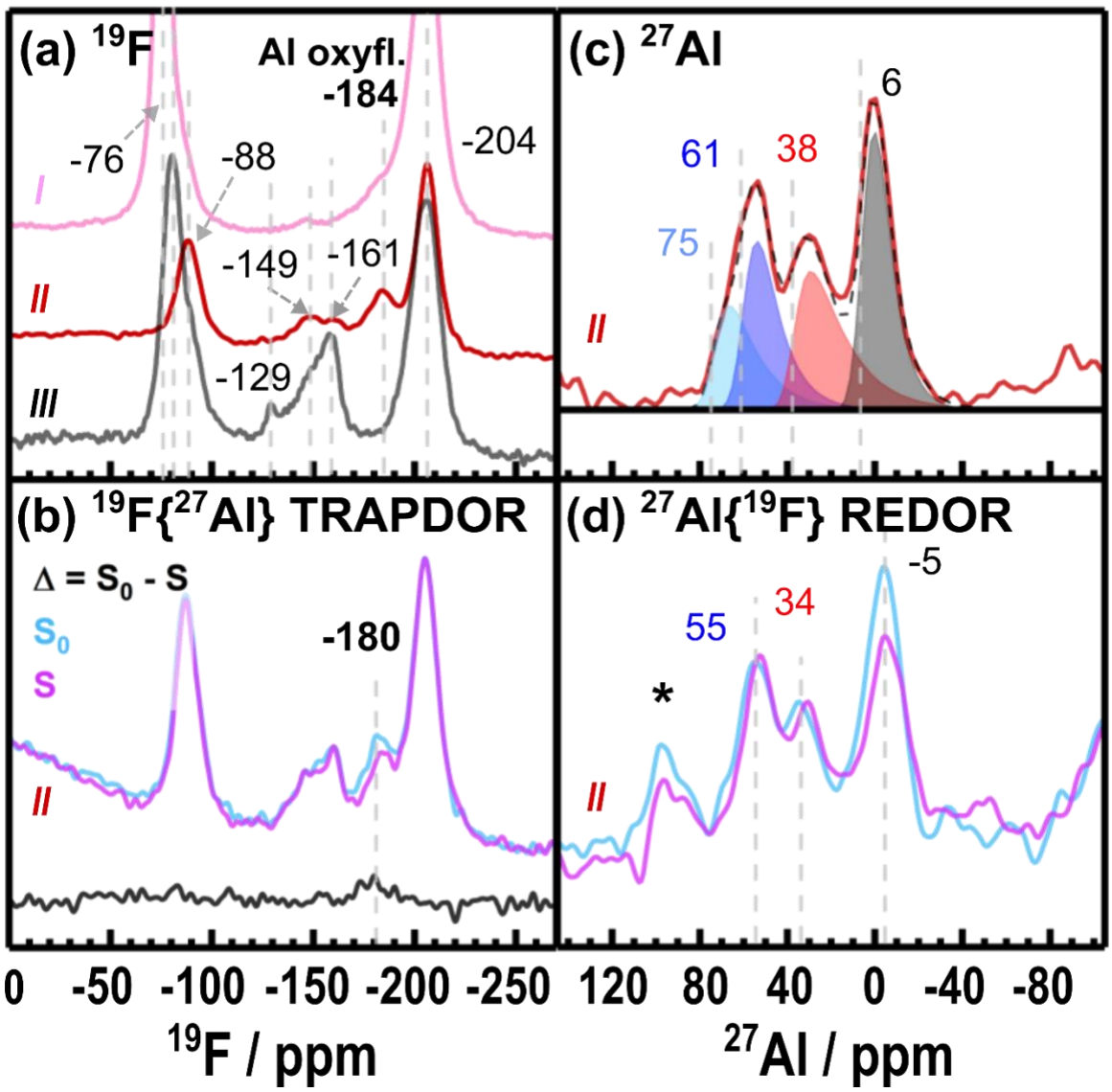

*Figure 5: The (a) ^{19}F MAS NMR (4.7 T, 50 kHz MAS, 250 ms recycle delay) of the three samples I, II and III presented in the voltage profile shown in Figure 3 (**a**). The $^{19}F\{^{27}Al\}$ TRAPDOR in (b) is for sample II (ALD NMC811 at 4.4 V_{Li}): a spectrum with no ^{27}Al adiabatic irradiation (S_0, cyan) over 25 μs dipolar evolution period and with ^{27}Al irradiation (S, magenta with 122 kHz ^{27}Al rf) for the same period are compared to yield a difference spectrum (Δ, black). Experiments with other dephasing times can be found in **ESI 5: Supporting NMR experiments**. In (c) is the corresponding ^{27}Al MAS NMR spectra of sample II acquired at 23.5 T. This spectrum is fitted using a Czjzek model with Al(IV), Al(V) and Al(VI) components plotted in blue (and cyan), red and black respectively. Isotropic chemical shifts of each fitted component are marked with a dashed line. The $^{27}Al\{^{19}F\}$ REDOR (23.5 T) in (d) shows the experiment without the ^{19}F irradiation (S_0, cyan) during the total dipolar evolution period of 269 μs and with ^{19}F π pulses (S, magenta) during the total dipolar evolution period. Spinning sideband are marked with asterisks (*).*

In the ALD NMC811 charged to 4.4 V_{Li} ^{19}F resonances belonging to the electrolyte salt, LiF and aluminium oxyfluoride are observed (point *II* in **Figure 3** (**a**)) too with the oxyfluoride signal higher in signal and better resolved than in the electrolyte-soaked sample. This reaffirms the greater extent of HF scavenging occurring with electrochemical cycling at high potentials due to the chemical oxidation of the solvent. Other resonances can also be resolved; resonances

at -129 and -149 ppm fall within the range of polymeric or silicon/boron fluorides (from reactions between HF and the glass fibre separator)[8,10] whilst -161 ppm is assigned to HF with hydrogen bonding.[8] The difference $^{19}F\{^{27}Al\}$ TRAPDOR spectrum (**Figure 5** (**b**)) of the charged sample (point *II*) shows a weak peak at -180 ppm, supporting the assignment of this resonance to an aluminium oxyfluoride species. None of the other peaks are attenuated (within the signal-to-noise of this experiment), indicating those are not associated with the coating.

The ^{27}Al NMR features in the charged sample (*II*, **Figure 5** (**c**)) show resonances at lower chemical shifts than the samples without exposure to $LiPF_6$ related products. $^{27}Al\{^{19}F\}$ REDOR (**Figure 5** (**d**)) shows a clearer attenuation in the signal of the Al(VI) site after the ALD NMC811 material has been charged to 4.4 V_{Li} (compared to the electrolyte-soaked sample in **Figure S13** (**c**)). These results are consistent with the $^{19}F\{^{27}Al\}$ TRAPDOR spectrum, confirming fluorination of the Al_2O_3 coating to form aluminium oxyfluoride species as the $LiPF_6$ salt undergoes hydrolysis to generate HF. The rate of hydrolysis is proposed to increase at high potentials due to the chemical oxidation of EC that produces water.[8–10,84]

Interestingly, fitting the ^{27}Al spectrum (**Figure 5** (**c**)) reveals a shoulder peak to the main Al(IV) environment at higher chemical shifts ($\bar{\delta}_{iso}$ = 75 ppm). This resonance contributes 17 % to the total signal (Al(IV):Al(V):Al(VI) ratios from this fit yield 41:27:32). The additional Al(IV) component was not clearly observed in the spectra of the uncycled materials acquired at lower fields amongst the three other major components. Fitting the ^{27}Al spectra of further electrochemically cycled samples indicates irreversibility of the structural evolution as the original Al(IV):Al(V):Al(VI) ratios (47:37:16) are never recovered and resonances remain at lower chemical shifts. Analysing the spectra (acquired at 16.4 T) of the ALD NMC811 in the discharged state (*IV*, **Figure S18** (**a**)), the Al(IV):Al(V):Al(VI) ratio of 48:18:34 whilst the sample charged to 4.4 V_{Li} on the second cycle (*V*, **Figure S18** (**b**)) had an Al(IV):Al(V):Al(VI) ratio of 44:14:42. Interestingly, secondary Al components ($\bar{\delta}_{iso} = 15$ ppm and $\bar{\delta}_{iso} > 70$ ppm) were only required when fitting spectra of samples charged to 4.4 V_{Li} (*II*, **Figure 5** (**c**) and *V*, **Figure S18** (**b**)), indicating these components may be SoC dependent and are not observed in the fully lithiated states (**Figure 2** (**a**-**c**) and *IV*, **Figure S18** (**a**)).

^{27}Al-^{7}Li double-resonance experiments were performed on the materials at high SoC to identify any lithiated alumina phases that could be attributed to the additional fitted components. The delithiated state also offers the additional benefit that the ^{7}Li signal of Li within the NMC811 structure is suppressed and the surface Li species will increasingly dominate. A shift in the ^{7}Li resonance to -0.4 ppm was observed in the ^{7}Li spectrum of the ALD NMC811 charged up to 4.4 V_{Li} in the second cycle (**Figure S19** (**c**)), which suggests that different species are present in the cycled ALD NMC811 sample compared to γ-$LiAlO_2$ (0.5 ppm). Negligible signal

attenuation of the -0.4 ppm ^{7}Li resonance was observed in the ^{7}Li{^{27}Al} TRAPDOR experiment (**Figure S19** (**c**)), using the same parameters as used for the reference material γ-$LiAlO_2$, indicating that weaker ^{7}Li-^{27}Al dipolar interactions are present in the ALD sample. A ^{27}Al{^{7}Li} REDOR experiment was performed (in which a train of ^{7}Li π pulses is applied, see **Figure S19** (**b** and **d**)) to explore these couplings further. The much stronger (21 %) signal attenuation of the ^{27}Al resonance of γ-$LiAlO_2$, compared to the cycled ALD NMC811 sample (where negligible attenuation was seen) supports the hypothesis of weaker ^{7}Li-^{27}Al interactions in the cycled ALD NMC811. Thus, these double resonance experiments are not consistent with the formation of a $LiAlO_2$-like phase in the coating during charge.

(iii) Electrolyte decomposition with at high potentials: gas evolution and solution NMR

The additional interactions with the electrolyte during early cycling stages by the ALD NMC811 at high potentials are probed by monitoring the electrolyte decomposition. *NMC811*|Li *operando* cells were cycled and the evolution profile of CO_2 (*purple*), CO (*pink*), O_2 (*blue*) and H_2 (*grey*) are presented in **Figure 6**.

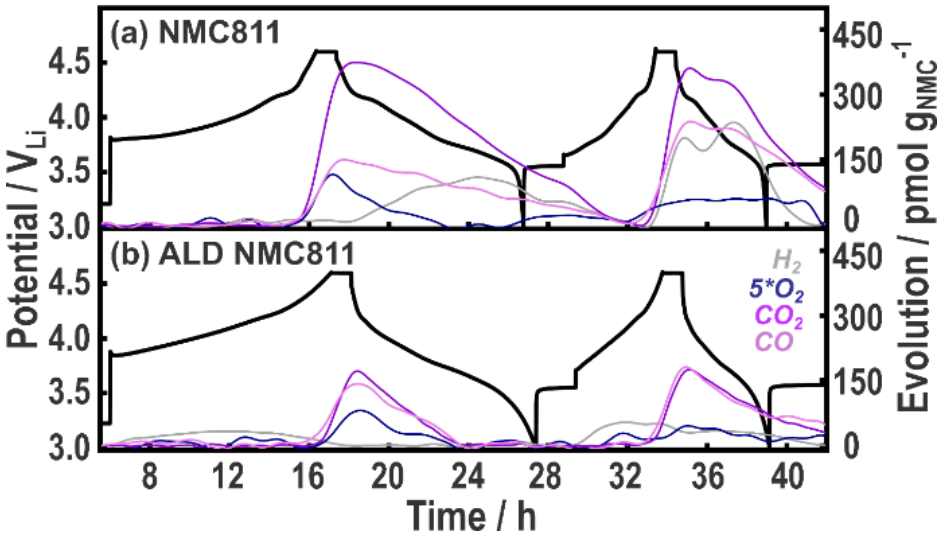

Figure 6: Online-electrochemical mass spectrometry (OEMS) and the corresponding voltage profiles of NMC811|Li (a) without and, (b) with an Al_2O_3 coating. Operando cells are cycled between 3 – 4.6 V_{Li} at a C/10 rate (assuming 200 $mAhg^{-1}$ practical capacity) with a 1 h hold at the top of charge and Ar being used as the carrier gas.

For NMC811, the ratio of CO:CO_2 at high potentials (~4.31 V_{Li} in **Figure 6** (**a**)) is approximately 1:2.5. This CO:CO_2 emission has previously been attributed to the chemical oxidation of carbonate solvents by either evolved singlet oxygen from the NMC811 surface reconstruction, or directly *via* reaction with surface oxygen.[8,9] The growth in gas evolved on cycle 2 (**Figure S20**) is proposed to be a result of increased surface area in these polycrystalline NMC811 particles as a result of cracking.[4] H_2 evolution has an onset potential after the CO/CO_2 evolution, suggesting that it originates from cross-talk and anodic reduction of soluble products generated during electrolyte oxidation at the NMC811 surface. On the other hand, the ALD

NMC811 electrode shows a 1:1.2 $CO:CO_2$ ratio in the first cycle (onset at ~4.41 V_{Li} in **Figure 6** (**b**)). The release of H_2 now precedes the onset of CO/CO_2, suggesting that soluble protic species are released by the coating (chemisorbed water/hydroxyls) at potentials lower than 4.3 V_{Li} (potentially reacting with $LiPF_6$ to form other acidic species), which are all reduced on the Li metal counter electrode. The presence of the coating reduces the total gas evolution associated with the chemical oxidation of the carbonate solvents, but results in the generation of more protic species at lower potentials.

The impact of the coating on electrolyte degradation was also analysed after electrochemical cycling at high potentials (3.0 - 4.6 V_{Li} with a 60 h hold at 4.6 V_{Li}, **Figure S25**) with solution NMR. Delithiated $LiFePO_4$ (LFP) was used as the counter electrode to avoid the reduction of any generated species due to its high operating potential of ~3.5 V_{Li}. Rinkel and co-workers have previously reported reactions between carbonate solvents in the electrolyte and reactive oxygen on the surface of layered transition metal oxides.[8,10] Linear carbonates readily undergo hydrolysis resulting in alcohols that can be chemically oxidised by the reactive oxygen to form aldehydes. These aldehydes can undergo hydrolysis by either alcohols or the water to acetals and these acetals can also react with the reactive oxygen to form carboxylic acids. ^{1}H NMR of the ALD NMC811 (**Figure S26** (**b**)) after one cycle shows Li formate/formic acid (8.25/8.19 ppm) whereas the uncoated NMC811 (**Figure S26** (**a**)) only shows acetals (5.69 and 5.80 ppm for methoxymethanol and methanediol respectively). After five cycles, the ^{1}H solution NMR (**Figure S27**) shows that the range and relative concentrations of solution degradation products (including alcohols, aldehydes, acetals and formic acid) are similar between the NMC811 and ALD NMC811. A detailed summary of the ^{1}H solution NMR assignments can be found in the **ESI 5: Supporting NMR experiments**. The apparent lack of impact of the coating on the degradation of the electrolyte from the perspective of solution NMR after more than one cycle is explored further in the discussion.

(iv) X-ray absorption spectroscopic analysis

The XAS spectra of (ALD) NMC811 in the pristine state and at the end of first charge up to 4.4 V_{Li} are compared with aged cells that have been charged back to 4.4 V_{Li} and then disassembled.

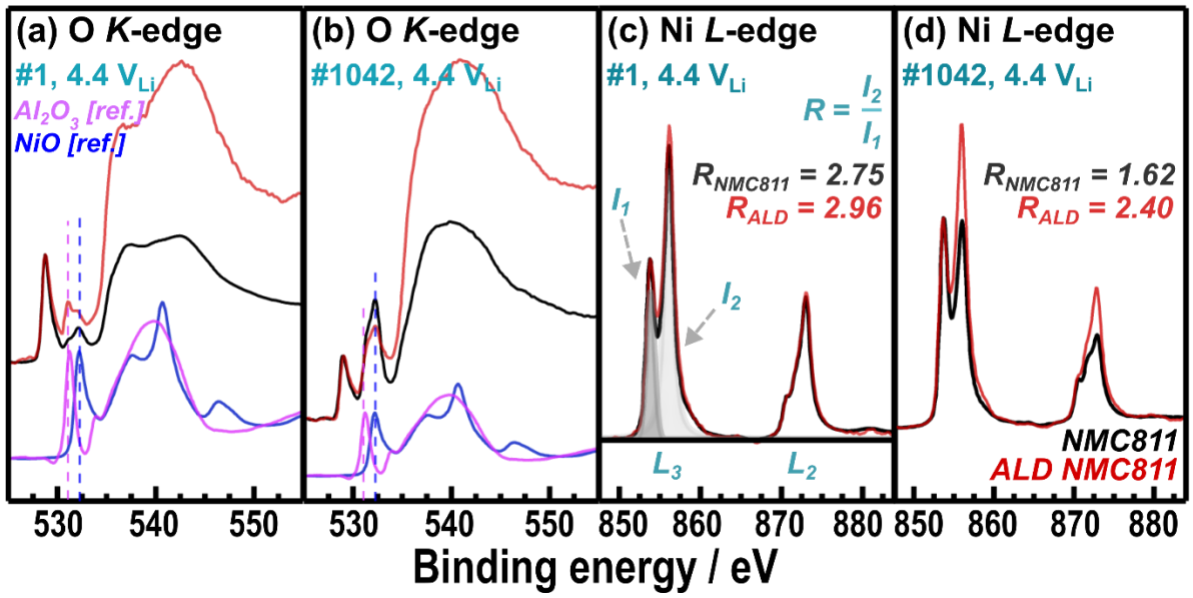

Figure 7: The O K-edge (a) and (c) Ni L-edge X-ray absorption spectroscopy of the NMC811 (black) and ALD NMC811 (red) electrodes charged to 4.4 V_{Li} on the first cycle are presented with spectra from reference samples of γ-Al_2O_3 (magenta) and NiO (blue). Dashed lines denote the O K-edge positions of the reference samples: 531.3 eV for γ-Al_2O_3 and 532.2 eV for NiO. O K-edge and Ni L-edge spectra of the materials in the electrochemically aged state (after cycle 1042) and charged up to 4.4 V_{Li} are presented in (b) and (d) respectively. Ratios of the L_3 high energy (I_2, 855.8 eV) : low energy (I_1, 853.7 eV) integrated areas are expressed with R for the Ni-Ledge.

The electronic state of the uncycled (ALD) NMC811 electrodes was first probed *via* Ni *L*-edge and O *K*-edge XAS in the total electron yield (TEY) mode. Two peaks (528.8 and 529.8 eV) previously assigned to the excitation of electrons from O 1*s* to the hybridised TM 3*d* - O 2*p* orbital are observed in the O *K*-edge (**Figure S23**).[88,89] A clear rise in the O *K*-edge pre-edge feature (531.3 eV) is also observed for the ALD NMC811, corresponding to a γ-Al_2O_3-like environment and confirming the presence of the coating. In the Ni *L*-edge (**Figure S24**), the main L_3 peak has two components; a low energy peak at 853.7 eV is associated with low-spin Ni^{3+} with a $3d^7$ electronic configuration (and to a lesser degree Ni^{4+} if present) whilst the higher energy peak at 855.8 eV is present for all Ni^{2+}, Ni^{3+} and Ni^{4+}.[90,91] The observed L_3 splitting (1.87 eV) for the uncycled (ALD) NMC811 is consistent with the covalent nature of the hybridised Ni 3*d* – O 2*p* bond.[92] As the 855.8 eV peak of the Ni *L*-edge is associated with oxidised Ni chemical states, the delithiated state of NMC811 (4.4 V_{Li}) is selected to maximise changes in this feature.

On the first charge up to 4.4 V_{Li}, the O *K*-edge spectra (**Figure 7** (**a**)) shows the peak corresponding to the excitation of O 1*s* electrons to the hybridised TM 3*d* – O 2*p* orbital (528.8 and 529.8 eV).[88,89] The O *K*-edge signature of γ-Al_2O_3-like environments (531.3 eV) is still present for the ALD NMC811. A new peak at 532.2 eV is observed for both the ALD NMC811 and uncoated NMC811 which is tentatively assigned to oxygen in reduced surface layers (during surface reconstruction)[91,93] since it matches with the reference NiO. The Ni L_3-edge

(**Figure 7** (**c**)) also evolves as the high energy feature (855.8 eV) becomes more prominent than the lower energy feature (853.7 eV), consistent with oxidation in the hybridised Ni 3*d* – O 2*p* bond.[89,94] Analysing the L_3 high energy:low energy (855.8 eV: 853.7 eV) area ratio ($\frac{I_2}{I_1}$ in **Figure 7** (**c**)) can therefore be a proxy for assessing the change of electron density in the hybridised Ni-O bond. The increased L_3 ratio of the (ALD) NMC811 is consistent with the reported oxidation of the hybridised Ni 3*d* – O 2*p* bond at high SoC.[89,92] **Table S15** compares the L_3 ratio for different SoC to highlight how a large L_3 ratio for samples in the charged state are an indicator of continued redox activity in the hybridised Ni 3*d* – O 2*p* bond. In addition, the growth in the L_3-L_2 splitting from 1.87 eV to 2.34 eV for the samples (with and without the Al_2O_3) with charging indicates an increase in the ionic nature of the hybridised bond.[92]

After extended electrochemical cycling, the O *K*-edge of the aged NMC811 charged to 4.4 V_{Li} (**Figure 7** (**b**)) differs from the first charge, with the 532.2 eV peak (assigned to NiO-like species) growing dramatically. This growth suggests that both the NMC811 and ALD NMC811 materials have undergone further surface reconstruction and degradation. In the Ni *L*-edge spectra (**Figure 7** (**d**)), extensive cycling resulted in smaller area ratios relative to early cycling life. The values complement the O *K*-edge analysis of the aged samples showing a more reduced surface Ni environment compared to the early cycle stages. However, the ALD NMC811 shows the least reduced environment as it has a relatively high area ratio of 2.40 (initially 2.96). The electronic density in the surface Ni-O bonds of the Al_2O_3-coated NMC811 therefore indicates electrochemical activity is preserved after the electrochemical ageing and less surface degradation has occurred in the presence of the Al_2O_3. This is in agreement with the higher available capacity for the ALD NMC811 after 1042 cycles (**Figure 3** (**b**)).

4. Discussion

(i) Evolution of the coating structure

Atomic layer deposition produces an amorphous Al_2O_3 coating on NMC811 with Al(IV), Al(V) and Al(VI) environments as seen by ^{27}Al NMR spectroscopy (**Figure 2** (**a**)). This disordered structure will contain Lewis acid sites (undercoordinated Al sites) – such sites are well-reported in so-called transition alumina phases (*e.g.* δ, η, γ- phases).[95–97] It should be noted that the uncoated NMC811 has pre-existing proton-containing species like (bi)carbonates, physisorbed water, LiOH and terminal hydroxyl groups on the transition metals (**Figure S7**). The ALD synthesis process inherently introduces new OH groups now within or on the coating as confirmed by the ^{27}Al{^{1}H} REDOR experiments (**Figure S9** (**a**)). A signal attenuation for all coordination environments indicates that Al^{3+} in all coordination environments in the coating are near ^{1}H.

Peri[71], Knözinger and Ratnasamy[98] have previously studied the ^{1}H resonances of transition alumina phases and proposed five types of hydroxylated Al surface environments (**Scheme 1**). Case I_a is for tetrahedral Al with a terminal OH group; case I_b is for octahedral Al with a terminal OH group, case II_a consisting of a hydroxyl group that bridges one tetrahedral and one octahedral Al, case II_b with a hydroxyl group bridging two octahedral Al, and finally case *III* with an OH bridging three octahedral Al. The ^{1}H chemical shift is extremely sensitive to the coordination number of the O in the O-H bond and the nature and number of Al ions coordinated it, along with any hydrogen bonding between clusters in aluminium hydroxide/aluminium oxide hydroxide phases.[72] The three 1st cation coordination sphere Al^{3+} ions (relative to the proton) found within the Al_3OH clusters are proposed to provide an induction effect that deshields these protons the most of all five cases (resulting in the most positive shift).[72] In addition, hydrogen bonding to a nearby oxygen also results in positive shifts: the shorter the H-bond, the larger the degree of deshielding: Piedra and co-workers showed that the Al_2OH clusters in Gibbsite $Al(OH)_3$ have interlayer hydrogen bonds of 1.98 Å and an associated ^{1}H resonance at 5.8 ppm, whilst environments with a longer intralayer hydrogen bonding (average of 2.3 Å) show resonances at 4.3 and 2.9 ppm.[72] Therefore the highest frequency ^{1}H resonances observed for the pristine ALD NMC811 (**Figure 2** (**d**)) at 9.5, 7.5 and 4.5 ppm are tentatively assigned to case *III* (Al_3OH clusters, 9.5 ppm *vs.* 10.8 ppm in Diaspore)[72] and lower frequency resonances at 7.5 and 4.5 ppm to case II_a (or case II_b) type sites (Al_2OH clusters), with varying degrees of H-bonding.

The Al sites in the ALD NMC811 show Lewis acidity[99–101] in allowing chemisorption of Lewis-base trace water onto the NMC811 after exposure to the solvent (or electrolyte). Non-dissociative adsorption of water onto an Al^{3+} Lewis acid site followed either by a reaction of more water or by dissociative chemisorption of the OH^- and H^+ has previously been proposed as the mechanism for this reaction (**Scheme 2**).[96,99] More generally, a model based on partial charges, entitled the multi-site complexation (MUSIC) model can be used to predict the affinity of a proton to bond to oxygen based on the expected electrostatic repulsion from nearby cation centres[102,103] and the partial charges contributed by each bonded cation to the Al-O bond (see discussion in **ESI 7: Multi-site complexation (MUSIC) model**. As such, the ability of the Al_2O_3 coating to sequester species like water from the electrolyte can be explained (using the MUSIC model as a framework) in terms of chemical characteristics of the coating *i.e.* the Lewis acid (undercoordinated Al) and Lewis basic (appropriate O) sites. **Scheme 2** illustrates one possible series of reactions (of many possible sequences of reactions) involving dissociative chemisorption of water, cleavage of Al-O bonds in a O_xAl-O-AlO_x cluster to form a new hydroxylated site (*red*, case *I* type Al_x-OH), and ultimately higher coordinate Al sites. Alternative mechanisms involving protonating nearby O (rather than Al-O-Al cleavage) are

also possible, since protonation of bridging oxygens between two Al(V) sites in Al_2OH clusters (Al-O-Al reported in dehydrated γ-Al_2O_3)[100] are more favourable than protonation of terminal hydroxyl oxygens (Al-OH). These bridging oxygens are more basic than the terminal hydroxyl oxygens when considering a simple model that is based on oxygen partial charges (see **ESI 7: Multi-site complexation (MUSIC) model**). However, the remaining undercoordinated Al site would be susceptible to further reactions with water as illustrated in **Scheme 2**, eventually forming two Al(VI) sites.

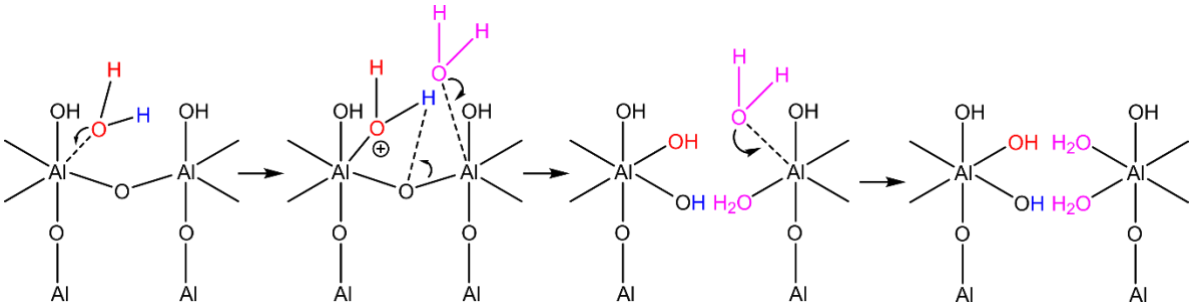

Scheme 2: One example illustrating how water could adsorb onto a Lewis acidic Al(V) site. The dissociation and subsequent chemisorption of the molecule fragments (OH^- in red and H^+ in blue) results in the formation of a new Al(VI) site with new hydroxyl groups and an Al(V) site which can further react with other Lewis bases (as indicated by two purple H_2O shown in the next steps). Additional hydroxyl groups not involved in the reaction are omitted.

These models are supported experimentally by the ^{27}Al NMR with an increase in Al(VI) sites from the pristine ALD NMC811 to the EC/EMC-soaked material (**Figure 2**) with chemisorption even of trace water. ^{27}Al{^{1}H} REDOR shows that the signal attenuation (from the ^{1}H-^{27}Al dipolar interactions) of the Al(IV), Al(V) and Al(VI) coordination sites changes depending on the sample state. In the pristine state, all Al^{3+} coordination sites are near ^{1}H (**Figure S9** (**a**)), but after the ALD NMC811 is soaked in the carbonate solvent and electrolyte, only the Al(VI) sites are close to ^{1}H (**Figure S9** (**c**) and **Figure S13** (**a**)). A concomitant change is observed in the normalised ^{1}H NMR (**Figure 2** (**d**) – (**f**)) with the signal intensity growing from 600 *a.u.* (case *II* (Al_2OH) at 4.5 ppm) to 1500 *a.u.* (case *I* ($Al_{VI}OH$) at 1.5 ppm) which is consistent with **Scheme 2**.

Soaking the ALD NMC811 in the electrolyte (1 M $LiPF_6$ in EC/EMC (3/7)) introduces acid-base reactions between the hydrated Al_2O_3 coating and species such as trace HF (generated upon PF_6^- hydrolysis). Fluorination of the coating is supported by the ^{27}Al resonances shifting to lower values (**Figure 2** (**c**), closer to AlF_3 at -17 ppm), some of the Al(VI) being fluoridated as shown *via* the ^{27}Al{^{19}F} REDOR spectrum in **Figure S13** (**c**)), and a ^{19}F resonance appearing at -180 ppm. Evidence of the involvement of protons from HF during this acid-base reaction is also reflected in the normalised ^{1}H signal intensity increasing to ~8000 a.u. (case *II*, Al_2OH at 5.8 ppm in **Figure 2** (**f**)). These ^{1}H protons are also close to Al(VI) sites as demonstrated in ^{27}Al{^{1}H} REDOR and ^{1}H{^{27}Al} TRAPDOR (**Figure S13** (**a**) – (**b**) respectively).

Two reaction mechanisms describing the HF scavenging reaction are presented below – **Scheme 3** (**I**) involves an increase in the coordination number of Al sites that neighbour hydroxylated 6-coordinated Al which can undergo neutralisation with HF. During neutralisation, an Al-F bond forms in place of the Al-OH with cleavage of this bond releasing a water molecule: Al-F is more thermodynamically favourable with a bond dissociation energy of 675 kJmol^{-1} compared to 547 kJmol^{-1} for Al-OH.[104] If there is a nearby under-coordinated site, the generated water can chemisorb to this site, thereby increasing the coordination number of that site and preventing further reactions triggered by "free" water. The second proton on the bound water has a greater affinity for bonding to bare bridging oxygens (in an Al-O-Al) than to the generated terminal Al-OH based on the simple MUSIC model analysis (**ESI 7: Multi-site complexation (MUSIC) model**). This first scheme therefore enables both the formation of protons in an Al_2OH environment (case *II*) and explains the fluorination of Al(VI).

DFT calculations by Tebbe *et al.* of both bare (in their case $LiCoO_2$) and alumina-coated surfaces[47] showed that an Al-F(-OH) environment is formed in the acid-base reaction between HF and an undercoordinated Al-OH site on the alumina surface. They found that, unlike reactions with TM-OH groups on the bare Co oxide surface, reactions between HF and an undercoordinated Al-OH site nearby an undercoordinated Al-F site generate two Al-F(-OH) sites, rather than releasing water (water release triggering further reactions). We note that the energies they calculate are based on the highly reactive three-coordinate Al species, which we do not be believe to be present (on the basis of our NMR experiments) and thus the driving forces maybe smaller than calculated. Our **second** proposed reaction type (**Scheme 3** (**II**)) is qualitatively similar to that of Tebbe *et al.*[47] and results in no change to the coordination number. The proton generated binds to an oxygen atom in a nearby AlO_x group and again no un-dissociated water is generated to cause further reactivity.

A chemical reaction (**Eq. 1**) is presented to describe the HF scavenging by the Al_2O_3 coating which is consistent with HF scavenging. It should be stressed that the illustrated mechanisms do not cover the full permutation space or possible reactivities, and further reactions between HF sites shown below likely also occur. However, the reactions do not proceed as far as to produce AlF_3.

$$Al_2O_2(OH)_2 + x\ HF \rightarrow Al_2O_2(OH)_{2-x}F_x(OH_2)_x \qquad \textit{Eq. 1}$$

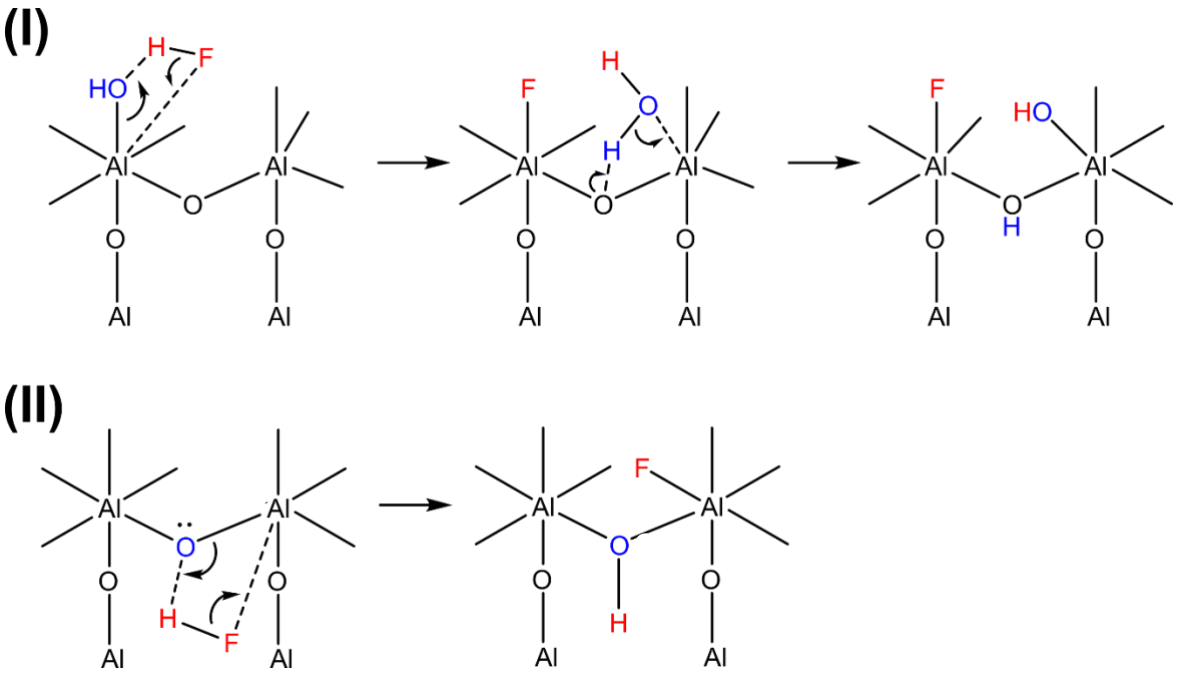

*Scheme 3: Two different scenarios in which HF scavenging could occur on the hydrated Al_2O_3 coating: (I) involves reaction with a terminal OH group that results in fluorination of an Al group with no change in coordination number but and an **increase** in the coordination number of a nearby Al site via water scavenging and (II) a reaction involving fluorination of an undercoordinated site to increase its coordination number. The mechanisms presented here are based on basicity arguments, Al-F bonds strengths and the DFT predictions from Tebbe and co-workers.[47]. Hydroxyl groups on the Al groups not involved in the reaction are omitted.*

A more well-defined ^{19}F signal (-184 ppm) for the Al oxyfluoride appears in the sample charged to 4.4 V_{Li} (**Figure 5** (**a**)) compared with the electrolyte-soaked material (**Figure 5** (**a**)). The reported chemical oxidation of EC by NMC811 at potentials > 4.3 V_{Li} that forms CO_2, CO and water[8–10,84] is verified in the gas evolution (**Figure 6** (**a**)). This water participates in hydrolysis of $LiPF_6$ to produce HF and this will react with the coating, forming more Al oxyfluoride than in the electrolyte-soaked state of the ALD NMC811. The chemisorbed protic species on the Al_2O_3 coating are not necessarily inactive with ion exchange between Li^+ and H^+ on the coating liberating protons into the electrolyte. H^+ (or H_3O^+) could diffuse to the Li counter electrode and electrochemically reduce during cycling of the ALD NMC811 as evidenced by H_2 evolution as soon as charging begins (**Figure 6** (**b**)). H_2 evolution was only detected at high potentials (> 4.3 V_{Li}) for the NMC811 when water was is generated (**Figure 6** (**a**)).

Fitting the ^{27}Al spectra of the ALD NMC811 at high SoC (*II*, **Figure 5** (**b**) and *V*, **Figure S18** (**b**)) showed additional minor Al(IV) and Al(VI) components ($\bar{\delta}_{iso,Al(IV)\,ii} > 70$ ppm and $\bar{\delta}_{iso,Al(VI)ii} = 15$ ppm). These were only required for in the charged state (not the sample discharged to 3.0 V_{Li}, *IV* in **Figure S18** (**a**)) and occur at higher chemical shifts than the major components (major components at $\bar{\delta}_{iso,Al(IV)\,i} \approx 61$ ppm and $\bar{\delta}_{iso,Al(VI)i} \approx 0$ ppm), indicating these environments are not fluorinated and there is some dependency of the Al local structure on SoC. Li^+-H^+ exchange on the coating is a chemical process, independent of electrochemical

cycling, so the apparent SoC dependency suggests Li^+-H^+ exchange is not the underlying cause. Two hypotheses to account for these observations are discussed.

One hypothesis is the lithiation of alumina to form a new phase during electrochemical cycling.[19,42,105,106] Since this cannot be a redox process it would have to involve Li^+-H^+ exchange and possibly structural rearrangements. In this study, reference γ-$LiAlO_2$ (82 ppm)[107] was compared to a cycled ALD NMC811 (charged to 4.4 V_{Li} on cycle 2) to test for lithiation; γ-$LiAlO_2$ is appropriate as it crystallises first from an amorphous state of precursor materials.[108] Unlike for the γ-$LiAlO_2$ sample (**Figure S19** (**a**) and (**b**)), the ^{7}Li-^{27}Al double resonance experiments of the ALD NMC811 charged up to 4.4 V_{Li} in second cycle showed very little evidence for any ^{27}Al-^{7}Li dipolar couplings and thus no close Li-Al proximity (**Figure S19** (**c**) and (**d**)). The magnitude of dipolar interactions (and thus signal attenuation when similar REDOR/TRAPDOR conditions are used) have an inverse cube relationship with the internuclear distance ($\propto 1/r^3$). γ-$LiAlO_2$ consists of LiO_4 tetrahedra corner shared with AlO_4 tetrahedra resulting in ^{27}Al-^{7}Li internuclear distances in the order of 3.09 or 3.17 Å (calculated from the structure).[109] Therefore the lack of signal attenuation for the ALD NMC811 charged to 4.4 V_{Li} in the second cycle in both REDOR and TRAPDOR indicates that any ^{27}Al-^{7}Li interactions present are likely occurring over distances much greater than 3.17 Å. It is thus unlikely that the ^{27}Al resonances at 70 and 15 ppm correspond to phases structurally related to γ-$LiAlO_2$ (83 ppm[110], r = 3.09 or 3.17 Å)[109], α-$LiAlO_2$ (17 ppm, r = 2.87 Å)[111] or $LiAl_5O_8$ with r = 2.76 Å.[112] Haber and co-workers also used ssNMR to investigate their Al-F based coating on $LiNi_{0.5}Mn_{1.5}O_4$.[42] They similarly performed ^{7}Li{^{19}F} and ^{27}Al{^{7}Li} REDOR experiments to investigate the nature of the Li ions formed on the surface upon electrochemical cycling, which suggested a proximity of these interfacial Li ions to both F and Al sites. The authors propose Li intercalation into the coating/the formation of Li-Al-O_x phases to explain their experimental observations. We note that their coatings are more highly fluorinated and there will be a stronger driving force for the more acidic protons in the $Al(OH)F_x$ groups to ion-exchange with Li (potentially also re-leaving protons), potentially explaining the differences between the two NMR studies.

Finally, the apparent SoC dependent resonances at higher chemical shifts ($\bar{\delta}_{iso,Al(IV)\,ii} > 70$ ppm and $\bar{\delta}_{iso,Al(VI)ii} = 15$ ppm) could be attributed to the effect of the paramagnetic ions on the Al ions at or on the NMC811-Al_2O_3 coating interface. These Al atoms, located within 5 Å of some $Ni^{2/3+}$ or $Mn^{3+/4+}$ cation centres, would experience *through-space* dipolar or *through-bond* interactions with unpaired electron density. However, reduced paramagnetism at high SoC (formally, Ni^{4+}) may enable the observation of some of these resonances and the apparent SoC dependent behaviour of the ^{27}Al spectra. Furthermore, some of these

resonances may simply have been buried under the major, undercoordinated Al(IV) environments, and they become more visible as the sites nearer the surface of the coating react with water and fluoride ions and their coordination environments increase.

(ii) Stabilisation of the surface environment

Previous DFT work on the surface stability of $LiNiO_2$ (considered the parent material for Ni-rich NMC) highlighted that there was significant covalency between the Ni 3*d* and O 2*p* orbitals. Determination of charge states using Wannier projections and subsequent treatment of the correlated states within dynamical mean-field theory shows little involvement of Ni in the redox process and a much larger involvement of O.[61] This is due to the highly entangled nature of the hybridised Ni-O bands and the high energy of the O 2*p* band relative to the Ni *d* orbitals.

Al appears to be responsible for a lowering of energies away from the Fermi edge in the DOS of surface O (**Figure 4 left**) compared to the uncoated case, whilst Bader charge analysis indicates an increase in the surface O charge with the Al (**Figure 4 right**). Both observations suggest that the coating reduces the covalency between Ni 3*d* and O 2*p*, for O ions that are also coordinated to Al. The coating helps to hinder the phase transformation of the delithiated layered structure (*e.g.* NiO_2) at high potentials to the more thermodynamically favourable rock salt (NiO) or rock salt like (Ni_3O_4) structure[9,61,113] concomitant with oxygen loss. The products of organic carbonate oxidation are a sign of reactive oxygen at the surface of the NMC811 particle.

Ni *L*-edge XAS provides experimental evidence of the stabilised surface with the Al_2O_3 coating when correlating features of the L_3 peak (ratio of I_2 peak at 855.8 eV and I_1 peak at 853.7 eV, $R = \frac{I_2}{I_1}$) to the health of the surface chemical state (capability to be redox active). In the first charge up to 4.4 V_{Li}, the coating does not affect the ratio ($R = \frac{I_2}{I_1} > 2.75$) and becomes the fingerprint for a charge transfer insulator in a mixed d^8L/d^8L^2 ligand hole state (**Figure 7** (**b**), *i.e.* ~$Li_{0.2}NiO_2$ in a non-degraded state). This notation is used rather than Ni^{3+}/Ni^{4+} to convey the oxidation of the hybridised Ni 3*d* – O 2*p* bond at high SoC. However, after electrochemical ageing, the uncoated NMC811 charged to 4.4 V_{Li} ($R = \frac{I_2}{I_1} = 1.62$) shows a dramatic difference to the ALD NMC811 ($R = \frac{I_2}{I_1} = 2.40$) in **Figure 7** (**b**). This suggests that the surface environment of the uncoated NMC811 can no longer achieve the oxidised d^8L/d^8L^2 state (~80 % delithiation), presumably due to surface reconstruction behaviour. In contrast, the ALD NMC811 shows preservation of the redox activity in the hybridised Ni-O bond. This implies that the additional charge on surface O, due to the presence of Al (**Figure 4 right**), has stabilised the surface against the $^1O_2$ evolution and surface reconstruction behaviour.

Further evidence for reactive surface oxygen and surface reconstruction behaviour being affected by the Al_2O_3 coating can also be tracked *via* gas evolution at high potentials (> 4.3 V_{Li}).[8,9,114] As detailed in the previous work by Jung and co-workers[9] and Rinkel and co-workers[8], the reactive oxygen is a strong electrophile can react with the organic carbonates (such as ethylene carbonate, EC). An overall reaction is presented in **Eq. 2**, where the formate formed in Eq. 3 continues to react further to generate a second CO_2 molecule and water. The water generated in this reaction can contribute to hydrolysis of the $LiPF_6$, adsorb to the NMC811 surface or hydrolyse the linear carbonate.[8]

OEMS measurements of the NMC811 (**Figure 6** (**a**)) show a $CO:CO_2$ ratio of 1:2.5 for the uncoated NMC811 in cycle 1 supporting the chemical oxidation reaction in **Eq. 2** – excess CO_2 from EC chemical oxidation has also been observed in the literature.[8,9] On the other hand, the lower volume of gases evolved for the ALD NMC811 is evidence that the coating has reduced the extent of EC chemical oxidation (**Figure 6** (**b**)). Furthermore, the $CO:CO_2$ ratio detected during electrochemical cycling of ALD NMC811 up to 4.6 V_{Li} was 1:1.2, indicating a different oxidation pathway or extent of oxidation. Jung and co-workers[9] previously suggested that the EC-intermediate formed from 1 mole of EC reacting with 1 mole of $^1O_2$ (**Eq. 3**) could decompose into 1 mole of CO, 1 mole of CO_2 and 1 mole of formaldehyde, but this reaction was not observed in their work. A lower extent of available oxidised oxygen sites in the presence of the Al_2O_3 coating may allow this reaction to out-compete the full reaction with both CH_2 groups in EC *via* **Eq. 2**.

$$EC + 2\,{}^1O_2 \rightarrow 2\,CO_2 + CO + 2\,H_2O \qquad \textit{Eq. 2}$$

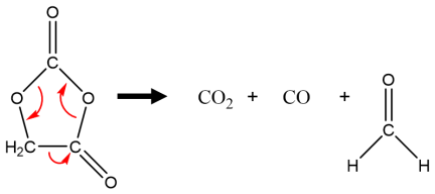

Eq. 3

Further evidence for this reaction could be found by looking for formaldehyde (and its by-products) in solution. However, formaldehyde is susceptible to further reactions in these Li-ion electrolyte systems with the release of $^1O_2$ from the NMC811. Rinkel and co-workers have reported that the formaldehyde can undergo hydrolysis to an acetal and the acetals subsequently react with reactive surface oxygen to produce formic acid/Li formate.[8] Formic acid can also be formed by direct oxidation of formaldehyde. After the first cycle, the uncoated NMC811 only showed acetals whereas the ALD NMC811 showed Li formate/formic acid (**Figure S26**). This appears to indicate oxidation of the aldehydes to the carboxylic acid[8,115–117] in the ALD NMC811, and not complete oxidation to form CO_2. However, extensive

electrochemical cycling resulted in minor differences between the ^{1}H solution NMR spectra of the uncoated and the Al_2O_3 coated NMC811 (**Figure S27**). This is ascribed to the fresh surfaces that form from the cracking caused by volume expansion and then contraction of NMC811 (~5 %)[118] during electrochemical cycling in polycrystalline NMC materials[4,5], resulting in dramatic increases of surface area. In some cases, charging polycrystalline materials to 4.4 V_{Li} resulted in a 200 % rise in surface area.[4] A growth in unprotected NMC811 surface that is exposed to electrolyte during the extended electrochemical cycling of the polycrystalline material could explain the lack of difference as the coating protection is a localised effect (**Figure 4**, **right**), and ultimately continued electrolyte oxidation even in the coated material.

Conclusion

In this work, a mechanistic understanding of the evolution of Al_2O_3 coatings on cathode material NMC811 and the effect on the NMC811 surface stability was developed. Solid-state NMR has been instrumental in highlighting the changing nature of the coating as it responds to trace water and HF in the electrolyte system. The capability to scavenge such species is highly dependent on the presence of undercoordinated cation sites – namely tetrahedrally and penta-coordinated Al sites in Al_2O_3 (as seen by ^{27}Al NMR) and the stronger Al-F *vs.* Al-OH bond. These sacrificial sites are important as water initiates a cycle of salt degradation that reduces the performance of Ni-rich layered oxides. Generation of water is especially concerning at high potentials for the Ni-rich layered oxides with oxidation of the electrolyte. Interestingly, the evidence indicates that *in-situ* formation of lithium aluminate upon electrochemical cycling does not occur.

The influence of the coating on the NMC811-electrolyte interactions was also demonstrated, with the coating lowering the amount and ratio of evolved CO and CO_2 gases observed on charging. These gases are associated with the reaction between EC and reactive oxygen at the surface of NMC811 during surface reconstruction behaviour. Oxidation of the hybridised Ni 3*d* – O 2*p* bonds above 75 % SoC generates reactive oxygen but different pathways to have been proposed to explain this degradation phenomenon of Ni-rich layered oxides.[61,113] This prompted analysis of Bader charges and the surface O density of states in this work. Both metrics indicated a decrease in covalency of the surface Ni 3*d* – O 2*p* hybridised bonds for O due to charge transfer from the bonded Al. The reduced covalency at high SoC indicates a lower probability of formation of ligand holes on O and hence a reduction in O loss. Therefore, it appears that the Al_2O_3 coating fundamentally increases the chemical stability of nearby surface oxygens (< 5 Å) by reducing hybridisation in the related Ni-O bonds. The localised protection offered by the coating could be expected to be compromised when degradation

phenomena like cracking in polycrystalline particles occurs and dramatic increases in unprotected surface area arise.

These results highlight the dual chemical role of Al_2O_3 coatings on NMC811: scavenging species in the electrolyte and the local passivation of surface oxygen. Extended cycling to high potentials for more than 1000 cycles confirms the importance of these protective mechanisms. Despite the initial lower capacity, the Al_2O_3 NMC811 retained ~71 % capacity (and higher absolute capacity after electrochemical ageing) compared to ~51 % for no coating. Such insights mean that careful material design choices are needed to optimise the benefits to electrochemical performance. Desired chemical characteristics of coatings are that the cations can favourably form fluorinated bonds while also scavenging water, and the chemical bonding to the NMC surface oxygen should be ionic in nature. Additionally, the morphology of the electrode material also plays a role, single crystals potentially benefiting over polycrystalline agglomerates, due to a much reduced tendency for crack formation thereby resulting in smaller increases in unprotected surface area.

Acknowledgements

This work was supported by the Faraday Institution degradation project (FIRG024, FIRG060). Samples were coated by Forge Nano with their proprietary atomic layer deposition process. R.L.B.C. gratefully acknowledges funding from the Cambridge Trust and the Cambridge Australia Scholarships. F.N.S. acknowledges funding from the Faraday Institution CATMAT project (FIRG016). H.B. acknowledges generous computing support provided by the CSD3 cluster of the University of Cambridge, Sulis HPC, Archer2 (access through Materials Chemistry Consortium), Michael cluster of UCL (Access through Faraday Institution Degradation project), and Brookhaven National Lab HPC Cluster (access through Centre for functional Nanomaterials). I.T. acknowledges support from a Beatriz Galindo senior fellowship (BG22/00148) from the Spanish Ministry of Science and Innovation. We thank Dr. Pardeep K. Thakur and Dr. Tien-Lin Lee for assistance with XAS experiments at the I-09 beamline of the Diamond Light Source, UK. R.L.B.C. also acknowledges the help from Dr. David Hall in initiating the collaboration with Forge Nano. The UK High-Field Solid-State NMR Facility is acknowledged for access to magnet time. Generous computing resources were provided by the Sulis HPC service (EP/T022108/1), and networking support by CCP-NC (EP/T026642/1), CCP9 (EP/T026375/1), and UKCP (EP/P022561/1).

References

1. Li, W., Erickson, E. M. & Manthiram, A. High-nickel layered oxide cathodes for lithium-based automotive batteries. *Nat Energy* **5**, 26–34 (2020).
2. Blomgren, G. E. The Development and Future of Lithium Ion Batteries. *J Electrochem Soc* **164**, A5019–A5025 (2017).
3. Grey, C. P. & Hall, D. S. Prospects for lithium-ion batteries and beyond—a 2030 vision. *Nat Commun* **11**, (2020).
4. Oswald, S., Bock, M. & Gasteiger, H. A. Elucidating the Implications of Morphology on Fundamental Characteristics of Nickel-Rich NCMs: Cracking, Gassing, Rate Capability, and Thermal Stability of Poly- and Single-Crystalline NCM622. *J Electrochem Soc* **169**, 050501 (2022).
5. Heenan, T. M. M. *et al.* Identifying the Origins of Microstructural Defects Such as Cracking within Ni-Rich NMC811 Cathode Particles for Lithium-Ion Batteries. *Adv Energy Mater* **10**, (2020).
6. Li, H. *et al.* An Unavoidable Challenge for Ni-Rich Positive Electrode Materials for Lithium-Ion Batteries. *Chemistry of Materials* **31**, 7574–7583 (2019).
7. Dose, W. M. *et al.* Onset Potential for Electrolyte Oxidation and Ni-Rich Cathode Degradation in Lithium-Ion Batteries. *ACS Energy Lett* 3524–3530 (2022) doi:10.1021/acsenergylett.2c01722.
8. Rinkel, B. L. D., Vivek, J. P., Garcia-Araez, N. & Grey, C. P. Two electrolyte decomposition pathways at nickel-rich cathode surfaces in lithium-ion batteries. *Energy Environ Sci* **15**, 3416–3438 (2022).
9. Jung, R., Metzger, M., Maglia, F., Stinner, C. & Gasteiger, H. A. Oxygen Release and Its Effect on the Cycling Stability of LiNi x Mn y Co z O 2 (NMC) Cathode Materials for Li-Ion Batteries . *J Electrochem Soc* **164**, A1361–A1377 (2017).
10. Rinkel, B. L. D., Hall, D. S., Temprano, I. & Grey, C. P. Electrolyte oxidation pathways in lithium-ion batteries. *J Am Chem Soc* **142**, 15058–15074 (2020).
11. Li, J. *et al.* The Impact of Electrolyte Additives and Upper Cut-off Voltage on the Formation of a Rocksalt Surface Layer in LiNi 0.8 Mn 0.1 Co 0.1 O 2 Electrodes . *J Electrochem Soc* **164**, A655–A665 (2017).
12. Steiner, J. D. *et al.* Accelerated Evolution of Surface Chemistry Determined by Temperature and Cycling History in Nickel-Rich Layered Cathode Materials. *ACS Appl Mater Interfaces* **10**, 23842–23850 (2018).
13. Dose, W. M., Xu, C., Grey, C. P. & De Volder, M. F. L. Effect of Anode Slippage on Cathode Cutoff Potential and Degradation Mechanisms in Ni-Rich Li-Ion Batteries. *Cell Rep Phys Sci* **1**, (2020).
14. David, L. *et al.* Unveiling the Role of Al2O3 in Preventing Surface Reconstruction during High-Voltage Cycling of Lithium-Ion Batteries. *ACS Appl Energy Mater* **2**, 1308–1313 (2019).
15. Karayaylali, P. *et al.* Coating-Dependent Electrode-Electrolyte Interface for Ni-Rich Positive Electrodes in Li-Ion Batteries. *J Electrochem Soc* **166**, A1022–A1030 (2019).

16. Mohanty, D. *et al.* Modification of Ni-Rich FCG NMC and NCA Cathodes by Atomic Layer Deposition: Preventing Surface Phase Transitions for High-Voltage Lithium-Ion Batteries. *Sci Rep* **6**, (2016).

17. Arumugam, R. S. *et al.* Special Synergy between Electrolyte Additives and Positive Electrode Surface Coating to Enhance the Performance of Li[Ni 0.6 Mn 0.2 Co 0.2]O 2 /Graphite Cells . *J Electrochem Soc* **163**, A2531–A2538 (2016).

18. Negi, R. S. *et al.* Insights into the Positive Effect of Post-Annealing on the Electrochemical Performance of Al2O3-Coated Ni-Rich NCM Cathodes for Lithium-Ion Batteries. *ACS Appl Energy Mater* **4**, 3369–3380 (2021).

19. Herzog, M. J., Gauquelin, N., Esken, D., Verbeeck, J. & Janek, J. Facile Dry Coating Method of High-Nickel Cathode Material by Nanostructured Fumed Alumina (Al2O3) Improving the Performance of Lithium-Ion Batteries. *Energy Technology* **9**, (2021).

20. Chen, Z. & Dahn, J. R. Studies of LiCoO2 Coated with Metal Oxides. *Electrochemical and Solid-State Letters* **6**, (2003).

21. Sun, Y. K., Lee, Y. S., Yoshio, M. & Amine, K. Synthesis and electrochemical properties of ZnO-coated LiNi0.5Mn1.5O4 spinel as 5 V cathode material for lithium secondary batteries. *Electrochemical and Solid-State Letters* **5**, (2002).

22. Kweon, H.-J. & Park, D. G. Surface Modification of LiSr 0.002 Ni 0.9 Co 0.1 O 2 by Overcoating with a Magnesium Oxide. *Electrochemical and Solid-State Letters* **3**, 128–130 (2000).

23. Cho, J., Kim, Y. J. & Park, B. Novel LiCoO2 cathode material with Al2O3 coating for a Li ion cell. *Chemistry of Materials* **12**, 3788–3791 (2000).

24. Cho, J., Kim, G. B., Lim, H. S., Kim, C.-S. & Yoo, S.-I. Improvement of Structural Stability of LiMn2O4 Cathode Material on 55°C Cycling by Sol-Gel Coating of LiCoO2. *Electrochemical and Solid-State Letters* **2**, 607–609 (1999).

25. Cho, J., Kim, Y. J. & Park, B. LiCoO2 Cathode Material That Does Not Show a Phase Transition from Hexagonal to Monoclinic Phase. *J Electrochem Soc* **148**, A1110 (2001).

26. Cho, Y. & Cho, J. Significant Improvement of LiNi0.8Co0.15Al0.05O2 Cathodes at 60°C by SiO2 Dry Coating for Li-Ion Batteries. *J Electrochem Soc* **157**, A625 (2010).

27. Lee, S. H., Yoon, C. S., Amine, K. & Sun, Y. K. Improvement of long-term cycling performance of Li[Ni0.8Co 0.15Al0.05]O2 by AlF3 coating. *J Power Sources* **234**, 201–207 (2013).

28. Herzog, M. J., Gauquelin, N., Esken, D., Verbeeck, J. & Janek, J. Increased Performance Improvement of Lithium-Ion Batteries by Dry Powder Coating of High-Nickel NMC with Nanostructured Fumed Ternary Lithium Metal Oxides. *ACS Appl Energy Mater* **4**, 8832–8848 (2021).

29. Zheng, L., Hatchard, T. D. & Obrovac, M. N. A high-quality mechanofusion coating for enhancing lithium-ion battery cathode material performance. *MRS Commun* **9**, 245–250 (2019).

30. Jung, Y. S. *et al.* Ultrathin direct atomic layer deposition on composite electrodes for highly durable and safe Li-Ion batteries. *Advanced Materials* **22**, 2172–2176 (2010).

31. Jung, Y. S. *et al.* Enhanced Stability of LiCoO[sub 2] Cathodes in Lithium-Ion Batteries Using Surface Modification by Atomic Layer Deposition. *J Electrochem Soc* **157**, A75 (2010).

32. Riley, L. A. *et al.* Electrochemical effects of ALD surface modification on combustion synthesized LiNi1/3Mn1/3Co1/3O2 as a layered-cathode material. *J Power Sources* **196**, 3317–3324 (2011).

33. Riesgo-González, V. *et al.* Effect of Annealing on the Structure, Composition, and Electrochemistry of NMC811 Coated with Al2O3 Using an Alkoxide Precursor. *Chemistry of Materials* (2022) doi:10.1021/acs.chemmater.2c02580.

34. Xu, G. L. *et al.* Building ultraconformal protective layers on both secondary and primary particles of layered lithium transition metal oxide cathodes. *Nat Energy* **4**, 484–494 (2019).

35. Ahn, J. *et al.* Ultrathin ZrO2 on LiNi0.5Mn0.3Co0.2O2 electrode surface via atomic layer deposition for high-voltage operation in lithium-ion batteries. *Appl Surf Sci* **484**, 701–709 (2019).

36. Xie, J. *et al.* Atomic Layer Deposition of Stable LiAlF4 Lithium Ion Conductive Interfacial Layer for Stable Cathode Cycling. *ACS Nano* **11**, 7019–7027 (2017).

37. Croy, J. R. *et al.* Insights on the Stabilization of Nickel-Rich Cathode Surfaces: Evidence of Inherent Instabilities in the Presence of Conformal Coatings. *Chemistry of Materials* **31**, 3891–3899 (2019).

38. Harper, A. F., Emge, S. P., Magusin, P. C. M. M., Grey, C. P. & Morris, A. J. Modelling amorphous materials via a joint solid-state NMR and X-ray absorption spectroscopy and DFT approach: application to alumina. *Chem Sci* **14**, 1155–1167 (2023).

39. Han, B. *et al.* Influence of Coating Protocols on Alumina-Coated Cathode Material: Atomic Layer Deposition versus Wet-Chemical Coating. *J Electrochem Soc* **166**, A3679–A3684 (2019).

40. Han, B. *et al.* Tailoring Alumina Based Interphases on Lithium Ion Cathodes. *J Electrochem Soc* **165**, A3275–A3283 (2018).

41. Han, B. *et al.* From Coating to Dopant: How the Transition Metal Composition Affects Alumina Coatings on Ni-Rich Cathodes. *ACS Appl Mater Interfaces* **9**, 41291–41302 (2017).

42. Haber, S. *et al.* Lithium exchange across a lithium-less coating for high energy cathodes. *J Power Sources* **560**, (2023).

43. Han, B. *et al.* Understanding the Role of Temperature and Cathode Composition on Interface and Bulk: Optimizing Aluminum Oxide Coatings for Li-Ion Cathodes. *ACS Appl Mater Interfaces* **9**, 14769–14778 (2017).

44. Myung, S. T. *et al.* Role of alumina coating on Li-Ni-Co-Mn-O particles as positive electrode material for lithium-ion batteries. *Chemistry of Materials* **17**, 3695–3704 (2005).

45. Chen, Z., Qin, Y., Amine, K. & Sun, Y. K. Role of surface coating on cathode materials for lithium-ion batteries. *J Mater Chem* **20**, 7606–7612 (2010).

46. Aykol, M., Kirklin, S. & Wolverton, C. Thermodynamic aspects of cathode coatings for lithium-ion batteries. *Adv Energy Mater* **4**, (2014).

47. Tebbe, J. L., Holder, A. M. & Musgrave, C. B. Mechanisms of LiCoO2 Cathode Degradation by Reaction with HF and Protection by Thin Oxide Coatings. *ACS Appl Mater Interfaces* **7**, 24265–24278 (2015).

48. Tesfamhret, Y., Younesi, R. & Berg, E. J. Influence of Al2O3 Coatings on HF Induced Transition Metal Dissolution from Lithium-Ion Cathodes. *J Electrochem Soc* **169**, 010530 (2022).

49. Dinnebier, R. E., Leineweber, A. & Evans, J. S. O. 2. The Rietveld method. in *Practical Powder Diffraction Pattern Analysis using TOPAS* 16–88 (De Gruyter, 2019). doi:doi:10.1515/9783110461381-002.

50. Coelho, A. TOPAS Academic. Preprint at (2015).

51. Chandran, C. V. *et al.* Alumina: Discriminative analysis using 3D correlation of solid-state NMR parameters. *Chem Soc Rev* **48**, 134–156 (2019).

52. Grey, C. P., Veeman, W. S. & Vega, A. J. Rotational echo 14N/13C/1H triple resonance solid-state nuclear magnetic resonance: A probe of 13C-14N internuclear distances. *J Chem Phys* **98**, 7711–7724 (1993).

53. Gullion, T. & Vega, A. J. Measuring heteronuclear dipolar couplings for I=1/2, S > 1/2 spin pairs by REDOR and REAPDOR NMR. *Prog Nucl Magn Reson Spectrosc* **47**, 123–136 (2005).

54. MacFarlane, D. R. *et al.* A Roadmap to the Ammonia Economy. *Joule* vol. 4 1186–1205 Preprint at https://doi.org/10.1016/j.joule.2020.04.004 (2020).

55. Lebens-Higgins, Z. *et al.* Electrochemical Utilization of Iron IV in the Li1.3Fe0.4Nb0.3O2 Disordered Rocksalt Cathode. *Batter Supercaps* **4**, 771–777 (2021).

56. Kresse, G. & Hafner, J. Ab initio molecular dynamics for liquid metals. *Phys Rev B* **47**, 558–561 (1993).

57. Kresse, G. & Furthmüller, J. Efficient iterative schemes for ab initio total-energy calculations using a plane-wave basis set. *Phys Rev B* **54**, 11169–11186 (1996).

58. Blöchl, P. E. Projector augmented-wave method. *Phys Rev B* **50**, 17953–17979 (1994).

59. Perdew, J. P., Burke, K. & Ernzerhof, M. Generalized Gradient Approximation Made Simple. *Phys Rev Lett* **77**, 3865–3868 (1996).

60. Perdew, J. P. *et al.* Restoring the Density-Gradient Expansion for Exchange in Solids and Surfaces. *Phys Rev Lett* **100**, 136406 (2008).

61. Genreith-Schriever, A. R. *et al.* Oxygen hole formation controls stability in LiNiO2 cathodes. *Joule* **7**, 1623–1640 (2023).

62. Liechtenstein, A. I., Anisimov, V. I. & Zaanen, J. Density-functional theory and strong interactions: Orbital ordering in Mott-Hubbard insulators. *Phys Rev B* **52**, R5467–R5470 (1995).

63. Dronskowski, R. & Bloechl, P. E. Crystal orbital Hamilton populations (COHP): energy-resolved visualization of chemical bonding in solids based on density-functional calculations. *J Phys Chem* **97**, 8617–8624 (1993).

64. Nelson, R. *et al.* LOBSTER: Local orbital projections, atomic charges, and chemical-bonding analysis from projector-augmented-wave-based density-functional theory. *J Comput Chem* **41**, 1931–1940 (2020).

65. Bader, R. F. W. Atoms in molecules. *Acc Chem Res* **18**, 9–15 (1985).

66. Lee, S. K., Park, S. Y., Yi, Y. S. & Moon, J. Structure and disorder in amorphous alumina thin films: Insights from high-resolution solid-state NMR. *Journal of Physical Chemistry C* **114**, 13890–13894 (2010).

67. Neuville, D. R., Cormier, L. & Massiot, D. Al environment in tectosilicate and peraluminous glasses: A 27Al MQ-MAS NMR, Raman, and XANES investigation. *Geochim Cosmochim Acta* **68**, 5071–5079 (2004).

68. d'Espinose de Lacaillerie, J. B., Fretigny, C. & Massiot, D. MAS NMR spectra of quadrupolar nuclei in disordered solids: The Czjzek model. *Journal of Magnetic Resonance* **192**, 244–251 (2008).

69. Trease, N. M. *et al.* Identifying the distribution of Al3+ in LiNi0.8Co0.15Al0.05O2. *Chemistry of Materials* **28**, 8170–8180 (2016).

70. Dogan, F., Vaughey, J. T., Iddir, H. & Key, B. Direct Observation of Lattice Aluminum Environments in Li Ion Cathodes LiNi1-y-zCoyAlzO2 and Al-Doped LiNixMnyCozO2 via 27Al MAS NMR Spectroscopy. *ACS Appl Mater Interfaces* **8**, 16708–16717 (2016).

71. Peri, J. B. A Model for the Surface of γ-Alumina. *J Phys Chem* **69**, 220–230 (1965).

72. Piedra, G., Fitzgerald, J. J., Dando, N., Dec, S. F. & Maciel, G. E. Solid-State 1H NMR Studies of Aluminum Oxide Hydroxides and Hydroxides. *Inorg Chem* **35**, 3474–3478 (1996).

73. Fitzgerald, J. J., Piedra, G., Dec, S. F., Seger, M. & Maciel, G. E. Dehydration Studies of a High-Surface-Area Alumina (Pseudo-boehmite) Using Solid-State 1 H and 27 Al NMR. *Journal of American Chemical Society* **119**, 7832–7842 (1997).

74. Borau-Garcia, J., Gutsulyak, D. V., Burford, R. J. & Piers, W. E. Selective hydration of nitriles to amides catalysed by PCP pincer supported nickel(ii) complexes. *Dalton Transactions* **44**, 12082–12085 (2015).

75. Yu, G., Hu, F., Huo, H., Ding, W. & Peng, L. Probing local structure of paramagnetic Ni-Al layered double hydroxides with solid-state 2H NMR spectroscopy. *Chem Phys Lett* **706**, 47–52 (2018).

76. Zhang, Z. *et al.* Unraveling the reaction mechanism of low dose Mn dopant in Ni(OH)2 supercapacitor electrode. *Journal of Energy Chemistry* **61**, 497–506 (2021).

77. Isobe, T., Watanabe, T., D'Espinose De La Caillerie, J. B., Legrand, A. P. & Massiot, D. Solid-state 1H and 27Al NMR studies of amorphous aluminum hydroxides. *J Colloid Interface Sci* **261**, 320–324 (2003).

78. Forsyth, M. & Macfarlane, D. R. *A Study of Hydrogen Bonding in Concentrated Diol/Water Solutions by Proton NMR. Correlations with Glass Formation*. *J. Phys. Chem* vol. 94 https://pubs.acs.org/sharingguidelines (1990).

79. Tsushima, S., Teranishi, K. & Hirai, S. Water diffusion measurement in fuel-cell SPE membrane by NMR. in *Energy* vol. 30 235–245 (Elsevier Ltd, 2005).

80. Ishihara, S. *et al.* Multinuclear solid-state NMR spectroscopy of a paramagnetic layered double hydroxide. *RSC Adv* **3**, 19857–19860 (2013).

81. Plakhotnyk, A. V., Ernst, L. & Schmutzler, R. Hydrolysis in the system LiPF 6 - Propylene carbonate - Dimethyl carbonate - H 2O. *J Fluor Chem* **126**, 27–31 (2005).

82. Campion, C. L., Li, W. & Lucht, B. L. Thermal Decomposition of LiPF6-Based Electrolytes for Lithium-Ion Batteries. *J Electrochem Soc* **152**, A2327 (2005).

83. Lebens-Higgins, Z. W. *et al.* Surface Chemistry Dependence on Aluminum Doping in Ni-rich LiNi0.8Co0.2−yAlyO2 Cathodes. *Sci Rep* **9**, (2019).

84. Jung, R., Metzger, M., Maglia, F., Stinner, C. & Gasteiger, H. A. Chemical versus electrochemical electrolyte oxidation on NMC111, NMC622, NMC811, LNMO, and conductive carbon. *Journal of Physical Chemistry Letters* **8**, 4820–4825 (2017).

85. Huang, H. *et al.* Unusual double ligand holes as catalytic active sites in LiNiO2. *Nat Commun* **14**, (2023).

86. Banerjee, H., Aichhorn, M., Grey, C. P. & Morris, A. J. Dynamic correlation driven paramagnetic insulating state and optical properties of the cathode material rhombohedral LiNiO2 at room temperature. *ChemRxiv* (2024).

87. Banerjee, H., Grey, C. P. & Morris, A. J. The stability and redox mechanisms of Ni-rich NMC cathodes: Insights from first-principles many-body calculations. *ChemRxiv* (2024).

88. Tian, C. *et al.* Depth-Dependent Redox Behavior of LiNi0.6Mn0.2Co0.2O2. *J Electrochem Soc* **165**, A696–A704 (2018).

89. Mirolo, M., Vaz, C. A. F., Novák, P. & El Kazzi, M. Multi-length-scale x-ray spectroscopies for determination of surface reactivity at high voltages of LiNi0.8Co0.15Al0.05O2vs Li4Ti5O12. *Journal of Chemical Physics* **152**, (2020).

90. DiMucci, I. M. *et al.* Scrutinizing formally Ni(IV) centers through the lenses of core spectroscopy, molecular orbital theory, and valence bond theory. *Chem Sci* (2023) doi:10.1039/D3SC02001K.

91. Björklund, E. *et al.* Cycle-Induced Interfacial Degradation and Transition-Metal Cross-Over in LiNi0.8Mn0.1Co0.1O2-Graphite Cells. *Chemistry of Materials* **34**, 2034–2048 (2022).

92. Wang, H. *et al.* Nickel L-edge soft X-ray spectroscopy of nickel-iron hydrogenases and model compounds - Evidence for high-spin nickel(II) in the active enzyme. *J Am Chem Soc* **122**, 10544–10552 (2000).

93. Yoon, W. S. *et al.* In situ soft XAS study on nickel-based layered cathode material at elevated temperatures: A novel approach to study thermal stability. *Sci Rep* **4**, (2014).

94. Wang, H. *et al.* L-edge sum rule analysis on 3d transition metal sites: From d10 to d0 and towards application to extremely dilute metallo-enzymes. *Physical Chemistry Chemical Physics* **20**, 8166–8176 (2018).

95. Ionescu, A., Allouche, A., Aycard, J. P., Rajzmann, M. & Hutschka, F. Study of γ-alumina surface reactivity: Adsorption of water and hydrogen sulfide on octahedral aluminum sites. *Journal of Physical Chemistry B* **106**, 9359–9366 (2002).

96. Coster, D. J., Fripiat, J. J., Muscas, M. & Auroux, A. Effect of Bulk Properties on the Rehydration Behavior of Aluminas. *Langmuir* **11**, 2615–2620 (1995).

97. John, C. S., Alma, N. C. M. & Hays, G. R. Characterization of transitional alumina by solid-state magic angle spinning aluminium NMR. *Appl Catal* **6**, 341–346 (1983).

98. Knozinger, H. & Ratnasamy, P. Catalytic Aluminas: Surface Models and Characterization of Surface Sites. *Catalysis Reviews* **17**, 31–70 (1978).

99. Ionescu, A., Allouche, A., Aycard, J.-P., Rajzmann, M. & Hutschka, F. Study of γ-Alumina Surface Reactivity: Adsorption of Water and Hydrogen Sulfide on Octahedral Aluminum Sites. *J Phys Chem B* **106**, 9359–9366 (2002).

100. Tsyganenko, A. A. & Mardilovichb, P. P. Structure of alumina surfaces. *J. Chem. Soc., Faraday Trans* 4843–4852 (1996).

101. Coster, D., Blumenfeld, A. L. & Fripiat, J. J. Lewis Acid Sites and Surface Aluminum in Aluminas and Zeolites: A High-Resolution NMR Study. *Journal of Physical Chemistry* **98**, 6201–6211 (1994).

102. Hiemstra, T., Venema, P. & Van Riemsdijk, W. H. Intrinsic Proton Affinity of Reactive Surface Groups of Metal (Hydr)oxides: The Bond Valence Principle. *J Colloid Interface Sci* **184**, 680–692 (1996).

103. Venema, P., Hiemstra, T., Weidler, P. G. & Van Riemsdijk, W. H. Intrinsic Proton Affinity of Reactive Surface Groups of Metal (Hydr)oxides: Application to Iron (Hydr)oxides. *J Colloid Interface Sci* **198**, 282–295 (1998).

104. Luo, Y.-R. *Handbook of Bond Dissociation Energies in Organic Compounds*. (CRC Press, 2002).

105. Jung, S. C. & Han, Y. K. How do Li atoms pass through the Al2O3 coating layer during lithiation in Li-ion batteries? *Journal of Physical Chemistry Letters* **4**, 2681–2685 (2013).

106. Liu, Y. *et al.* In situ transmission electron microscopy observation of pulverization of aluminum nanowires and evolution of the thin surface Al2O3 layers during lithiation-delithiation cycles. *Nano Lett* **11**, 4188–4194 (2011).

107. Müller, D., Gessner, W. & Scheler, G. *Chemical Shift and Quadrupole Coupling of the 27Al NMR Spectra of LiAlO2 Polymorphs*. *Polyhedron* vol. 2 (1983).

108. Isupov, V. P. *et al.* Mechanochemical synthesis of γ-LiAlO 2 studied by 6Li and 27Al NMR and synchrotron X-ray diffraction. *Inorganic Materials* **47**, 763–767 (2011).

109. Wiedemann, D. *et al.* Single-crystal neutron diffraction on γ-LiAlO2: Structure determination and estimation of lithium diffusion pathway. *Z Kristallogr Cryst Mater* **231**, 189–193 (2016).

110. Müller, D., Gessner, W. & Scheler, G. Chemical shift and quadrupole coupling of the 27Al NMR spectra of LiAlO2 polymorphs. *Polyhedron* **2**, 1195–1198 (1983).

111. Marezio, M. & Remeika, J. P. High-pressure synthesis and crystal structure of α-LiAlO2. *The Journal of Chemical Physics* vol. 44 3143–3144 Preprint at https://doi.org/10.1063/1.1727203 (1966).

112. Famery, R. & Queyroux, F. Etude structurale de la forme ordonnbe de LiAlsOs. *J Solid State Chem* **30**, 257–263 (1979).

113. Páez Fajardo, G. J. *et al.* Synergistic Degradation Mechanism in Single Crystal Ni-Rich NMC//Graphite Cells. *ACS Energy Lett* **8**, 5025–5031 (2023).

114. Zhang, Y. *et al.* Revealing electrolyte oxidation: Via carbonate dehydrogenation on Ni-based oxides in Li-ion batteries by in situ Fourier transform infrared spectroscopy. *Energy Environ Sci* **13**, 183–199 (2020).

115. Jørgensen, B., Egholm Christiansen, S., Dahl Thomsen, M. L. & Christensen, C. H. Aerobic oxidation of aqueous ethanol using heterogeneous gold catalysts: Efficient routes to acetic acid and ethyl acetate. *J Catal* **251**, 332–337 (2007).

116. Zope, B. N., Hibbitts, D. D., Neurock, M. & Davis, R. J. Reactivity of the Gold/Water Interface During Selective Oxidation Catalysis. *Science (1979)* **330**, 74–78 (2010).

117. Popova, G. Ya., Andrushkevich, T. V, Chesalov, Yu. A. & Stoyanov, E. S. In situ FTIR Study of the Adsorption of Formaldehyde, Formic Acid, and Methyl Formiate at the Surface of TiO2 (Anatase). *Kinetics and Catalysis* **41**, 805–811 (2000).

118. Märker, K., Reeves, P. J., Xu, C., Griffith, K. J. & Grey, C. P. Evolution of Structure and Lithium Dynamics in LiNi0.8Mn0.1Co0.1O2 (NMC811) Cathodes during Electrochemical Cycling. *Chemistry of Materials* **31**, 2545–2554 (2019).

119. Witt, E., Nakhal, S., Chandran, C. V., Lerch, M. & Heitjans, P. NMR and Impedance Spectroscopy Studies on Lithium Ion Diffusion in Microcrystalline γ-LiAlO2. *Zeitschrift fur Physikalische Chemie* **229**, 1327–1339 (2015).

120. Morris, H. D. & Ellis, P. D. 27A Cross Polarization of Aluminas. The NMR Spectroscopy of Surface Aluminum Atoms. *J. Am. Chem. Soc* **111**, 6045–6049 (1989).

121. Muller, D., Gessner, W., Behrens, H.-J. & Scheler, G. Determination of the aluminium coordination in aluminium-oxygen compounds by solid-state high-resolution 27Al NMR. *Chemical Physical Letters* **79**, 59–62 (1981).

122. Lacassagne, V. *et al.* Structure of high-temperature NaF-AlF3-Al2O3 melts: A multinuclear NMR study. *Journal of Physical Chemistry B* **106**, 1862–1868 (2002).

123. Chupas, P. J., Corbin, D. R., Rao, V. N. M., Hanson, J. C. & Grey, C. P. A combined solid-state NMR and diffraction study of the structures and acidity of fluorinated aluminas: Implications for catalysis. *Journal of Physical Chemistry B* **107**, 8327–8336 (2003).

124. Dressler, M. *et al.* Aluminum speciation and thermal evolution of aluminas resulting from modified Yoldas sols. *J Solid State Chem* **180**, 2409–2419 (2007).

125. Alemany, L. B. & Kirker, G. W. First Observation of 5-Coordinate Aluminum by MAS 27Al NMR in Well-Characterized Solids. *Journal of American Chemical Society* **108**, 6158–6162 (1986).

126. Lee, S. K., Park, S. Y., Yi, Y. S. & Moon, J. Structure and disorder in amorphous alumina thin films: Insights from high-resolution solid-state NMR. *Journal of Physical Chemistry C* **114**, 13890–13894 (2010).

127. Lippmaa, E., Samoson, A. & Mági, M. High-Resolution 27Al NMR of Aluminosilicates. *Journal of American Chemical Society* **108**, 1730–1735 (1986).

128. Delmas, C., Carlier, D., Ceder, G., Ménétrier, M. & Grey, C. P. Understanding the NMR shifts in paramagnetic transition metal oxides using density functional theory calculations. *Phys Rev B Condens Matter Mater Phys* **67**, (2003).

129. Iuga, D., Schäfer, H., Verhagen, R. & Kentgens, A. P. M. Population and Coherence Transfer Induced by Double Frequency Sweeps in Half-Integer Quadrupolar Spin Systems. *Journal of Magnetic Resonance* **147**, 192–209 (2000).

130. Gottlieb, H. E., Kotlyar, V. & Nudelman, A. NMR Chemical Shifts of Common Laboratory Solvents as Trace Impurities. *Journal of Organic Chemistry* **62**, 7512–7515 (1997).

131. Leskes, M., Moore, A. J., Goward, G. R. & Grey, C. P. Monitoring the electrochemical processes in the lithium-air battery by solid state NMR spectroscopy. *Journal of Physical Chemistry C* **117**, 26929–26939 (2013).

132. Massiot, D. *et al.* Modelling one- and two-dimensional solid-state NMR spectra. *Magnetic Resonance in Chemistry* **40**, 70–76 (2002).

133. Pauling, L. The Principles Determining the Structure of Complex Ionic Crystals. *J Am Chem Soc* **51**, 1010–1027 (1929).